

# Prediction of the daily spatial variation of stem water potential in cherry orchards using weather and Sentinel-2 data

Francisco Zambrano<sup>a,b</sup>, Abel Herrera<sup>a</sup>, Mauricio Olguín<sup>c,d</sup>, Miro Miranda<sup>e</sup>, Jesica Garrido<sup>a</sup>, Andrea Miyasaka Almeida<sup>c,d</sup>

<sup>a</sup>Hemera Centro de Observación de la Tierra, Facultad de Ciencias, Escuela de Ingeniería en Medio Ambiente y Sustentabilidad, Universidad Mayor, Santiago, Chile.

<sup>b</sup>Observatorio de Sequía para la Agricultura y la Biodiversidad de Chile (ODES), Universidad Mayor, Santiago, Chile.

<sup>c</sup>Centro de Genómica y Bioinformática, Facultad de Ciencias, Ingeniería y Tecnología, Universidad Mayor, Santiago 8580745, Chile.

<sup>d</sup>Escuela de Agronomía, Facultad de Ciencias, Ingeniería y Tecnología, Universidad Mayor, Santiago 8580745, Chile.

<sup>e</sup>German Research Center for Artificial Intelligence (DFKI) Kaiserslautern, Germany

Corresponding author. Email: [francisco.zambrano@umayor.cl](mailto:francisco.zambrano@umayor.cl)

This paper is a non-peer reviewed preprint submitted to EarthArXiv.

## Abstract

The common practice for irrigation management is to apply the water lost by evapotranspiration. However, we could manage the irrigation by monitoring the plant's water status by measuring the stem water potential ( $\Psi_s$ ), which is currently costly and time-consuming. The primary goal of this work is to predict the daily spatial variation of  $\Psi_s$  using machine learning models. We measured  $\Psi_s$  in two orchards planted with sweet cherry tree variety Regina, and we monitored 30 trees weekly and biweekly in the central part of Chile, during two seasons, 2022-2023 and 2023-2024, and between October and April. To predict the  $\Psi_s$ , we used the random forest (RF), extreme gradient boosting (XGBoost), and support vector machine (SVM) models. We selected vapor pressure deficit (VPD), reference evapotranspiration (ET<sub>0</sub>), relative humidity, and temperature as weather predictors. Also, we used as predictors spectral vegetation indices (VIs) and biophysical parameters derived from Sentinel-2. We compared two schemes, one for estimation and another for prediction. We discovered that XGboost and RF worked best for both. The estimation had an R<sup>2</sup> of 0.76 and an RMSE of 0.24 MPa. The prediction, on the other hand, had an R<sup>2</sup> of 0.59 and an RMSE of 0.36 MPa. The analysis of importance variables reveals that weather predictors, such as VPD, ET<sub>0</sub>, and temperature, have a higher weight in the model. These are followed by VIs that use short-wave infrared regions, which highlight the moisture stress index (MSI) and the disease and water stress index (DWSI).

## 1. Introduction

Climate change is increasingly recognized as a major driver of global water scarcity, exacerbating drought conditions and challenging water resources worldwide (Masson-Delmotte et al., 2021). This phenomenon has heightened concerns about agricultural sustainability and food security (Molotoks et al., 2021), as the agricultural sector is particularly vulnerable to changes in precipitation patterns and rising temperatures (Fernández et al., 2023; Zambrano et al., 2016). In recent years, the central and northern regions of Chile have experienced severe reductions in water availability (Garreaud et al., 2017; Zambrano et al., 2024), with profound implications for agricultural productivity (Zambrano, 2023). The ongoing drought in Chile has intensified the need for efficient water use in agriculture (Zúñiga et al., 2021), particularly in fruit orchards, which are highly dependent on

44 consistent and adequate irrigation to maintain productivity and quality (Liu et al., 2023;  
45 Vicente-Serrano et al., 2020). Efficient water management is thus crucial not only for reducing water  
46 consumption, but also for optimizing plant health and maximizing yields under water-limited  
47 conditions (D'Odorico et al., 2020). This, in turn, aids in our adaptation to a changing climate where  
48 water resources are limited in certain areas.

49 To ensure efficient irrigation, the plant must replenish both the water lost through transpiration and  
50 the moisture removed from the soil by weather conditions, a process known as evapotranspiration  
51 (ET) (Allen et al., 1998). However, calculating ET in the field can be challenging. Two of the most  
52 precise methods are eddy covariance stations or water balances (Denager et al., 2020), which are  
53 costly and thus not used by the average farmer. In consequence, the ET is generally estimated by  
54 calculating the reference evapotranspiration (ET<sub>0</sub>), also known as atmospheric evaporative demand  
55 (Shirmohammadi-Aliakbarkhani and Saberali, 2020). ET<sub>0</sub> can be roughly estimated from pan  
56 evaporation measuring the water loss, but the most common methods rely on meteorological data.  
57 The Food And Agriculture Organization (FAO) Penman-Monteith method is recommended as the  
58 standard for calculating ET<sub>0</sub> when sufficient weather data is available (Allen et al., 1998). When only  
59 temperature data is accessible, the Hargreaves-Samani method (Hargreaves and Samani, 1985) has  
60 shown good performance compared to the FAO Penman-Monteith method (Vicente-Serrano et al.,  
61 2007). Once the ET<sub>0</sub> is calculated, it must be adjusted to ET by multiplying it by the crop coefficient  
62 ( $K_c$ ), which varies depending on the crop type, growth stage, and condition, with tabulated values  
63 available (Allen et al., 1998). Despite their widespread use, these methods often lack spatial  
64 precision and may not account for variations in soil and plant water status across different orchard  
65 blocks, potentially leading to over- or under-irrigation (Jones, 2004). Furthermore, relying on  
66 generalized crop coefficients might not adequately capture the dynamic water needs of trees under  
67 varying environmental conditions, underscoring the need for more site-specific irrigation strategies.

68 To optimize irrigation, some studies have used regulated deficit irrigation (RDI), which consists of  
69 subjecting the plant to levels of water stress in different phenological stages (Yang et al., 2022). We  
70 can accomplish this by recovering by irrigation a portion of the ET that the plant has lost. To ensure  
71 good production and quality, irrigation typically recovers 100% of ET. Using RDI, we assess how the  
72 plant reacts physiologically and in terms of production and quality during specific phenological stages  
73 (Vélez-Sánchez et al., 2021). Alternatively, we could apply RDI and manage the irrigation based on  
74 the plant's response. For this, we can measure the plant's water potential (Corell et al., 2020). The  
75 water potential has been widely recognized as a reliable indicator of plant water status and a  
76 valuable tool for guiding irrigation decisions (Moriana et al., 2012; Naor, 2000). The solute  
77 concentration and water pressure in the leaf or stem directly show the water tension inside the  
78 plant, which is also called water potential. The water potential reflects the impact of soil water  
79 content, atmospheric water demand, and the plant's physiological responses (García-Tejera et al.,  
80 2021). Typically, we measure the water potential on the leaf, known as the leaf water potential, and  
81 on the stem, known as the stem water potential. In the latter case, the leaf is put into a plastic bag  
82 and sealed with the aim that the leaf potential equilibrates with the water potential of the stem  
83 (Levin, 2019). The water potential usually is taken at different times during the day; when the  
84 measure is made around 12:00-14:00, it corresponds to midday stem water potential ( $\Psi_s$ ). This  
85 range time corresponds to the maximum evaporative demand; thus, the  $\Psi_s$  tried to capture the  
86 water status of the plant at the highest stress time. This measurement has demonstrated  
87 consistency and reliability across various species (Carrasco-Benavides et al., 2022; Garofalo et al.,

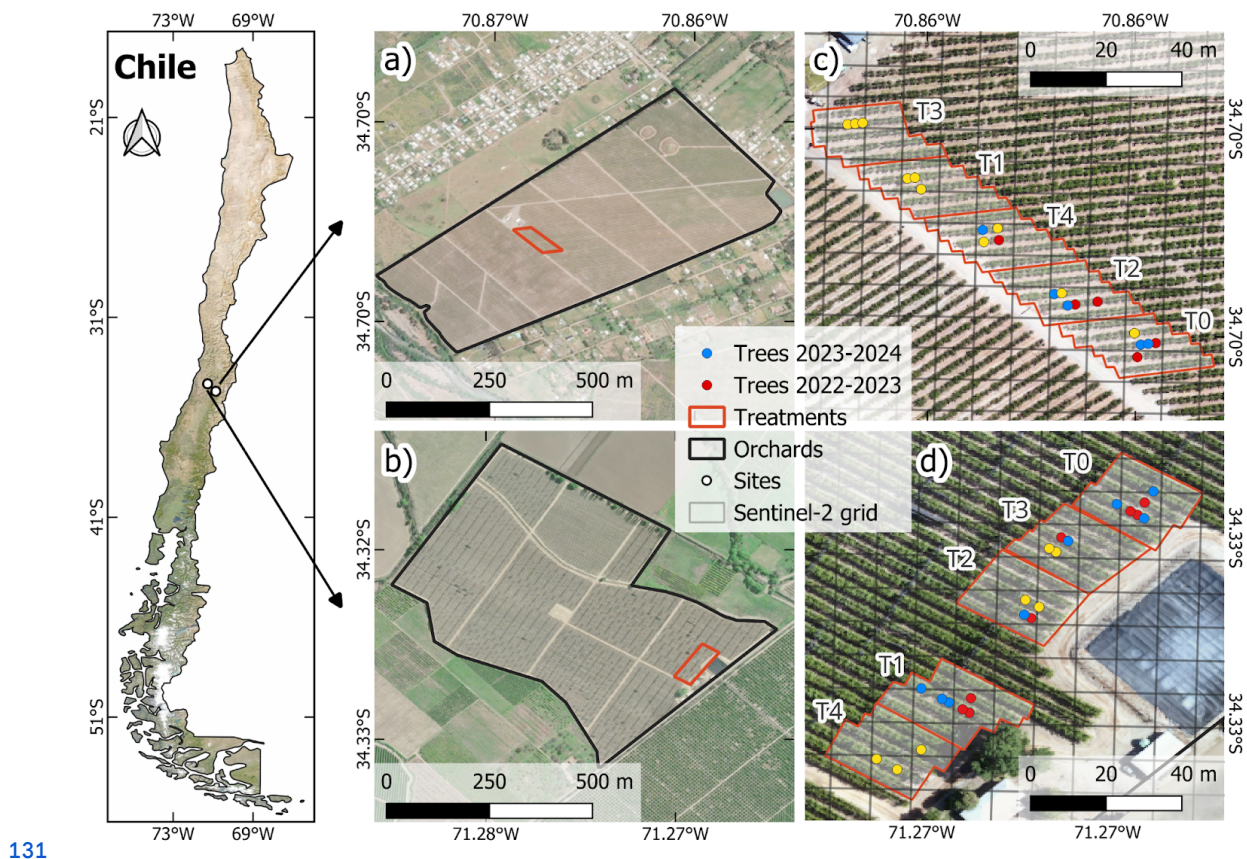
88 2023; Moriana et al., 2012). The  $\Psi_s$  vary during the season according to environmental factors and  
89 the irrigation applied, which reflects the plant water status. The major drawback of measuring  $\Psi_s$ , is  
90 that traditional methods, such as using a pressure chamber (Scholander et al., 1964), are  
91 labor-intensive, time-consuming, and not suitable for continuous monitoring or large-scale  
92 application (Jones, 2004).

93 New developments in remote sensing and modeling have made it possible to indirectly estimate  $\Psi_s$ ,  
94 by combining spectral and weather data with machine learning methods. This provides a scalable  
95 solution for managing irrigation in real time (Carrasco-Benavides et al., 2022; Garofalo et al., 2023;  
96 Savchik et al., 2024). Savchik et al. (2024) predicted  $\Psi_s$  in almond orchards, using ET, soil moisture,  
97 and spectral reflectance from unmanned aerial vehicles (UAV). They used the machine learning  
98 algorithms of random forests and neural networks. They reached  $R^2$  values ranging from 0.33 to 0.73  
99 and a root mean square error (RMSE) between 3.31 and 2.5 bars. In Italy, in an orchard of olives,  
100 Garofalo et al. (2023) used random forests to estimate  $\Psi_s$  based on vegetation indices derived from  
101 spectral data from PlanetScope imagery, reaching an  $R^2$  of 0.78. However, when used to predict in an  
102 independent year, the results decreased significantly. Carrasco-Benavides et al. (2022) used infrared  
103 thermal imagery from UAV and derived the crop water stress index (CWSI). They used artificial  
104 neural networks to estimate  $\Psi_s$  in cherry-tree variety Regina. The test data produced a Pearson  
105 correlation value of 0.83, but the absence of independent selection may have inflated the values.  
106 These technologies provide the potential to enhance decision-making processes by enabling more  
107 precise and timely irrigation interventions based on the actual water needs of the crop. Remote  
108 sensing technologies have emerged as powerful tools for enhancing irrigation management by  
109 providing spatially detailed information on crop water status and variability across large areas  
110 (Zarco-Tejada et al., 2003). Sentinel-2 (S2), with its high spatial resolution and frequent revisit times,  
111 offers the ability to monitor vegetation by spectral indices, canopy cover, and thermal status, which  
112 are proxies of plant water stress (Addabbo et al., 2016; Jamshidi et al., 2021; Zhang et al., 2017).  
113 These indices, derived from multispectral imagery, can be used to assess crop water needs and  
114 optimize irrigation schedules more accurately than traditional methods. By integrating remote  
115 sensing data with weather and soil moisture measurements, it is possible to develop advanced  
116 irrigation management systems that respond dynamically to the actual water status of the crop,  
117 improving water use efficiency and crop performance (Baluja et al., 2012).

118 In this study, we aim to investigate the potential of using S2 and weather data to predict the daily  
119 spatial variation of  $\Psi_s$  in cherry orchards. To achieve this, we define three specific goals: i) to derive  
120 daily spatial predictors from S2 and weather stations; ii) to train and evaluate three machine  
121 learning models; and iii) to evaluate the spatio-temporal variation of estimated  $\Psi_s$  for monitoring  
122 irrigation. For this, we use satellite S2 (A/B) and weather data to derive multiple predictors.  
123 Following, we evaluate three machine learning algorithms: random forest (RF), extreme gradient  
124 boosting (XGBoost), and support vector machines (SVM). We use two splitting strategies,  
125 considering time and space, to obtain training and testing datasets. On the training dataset, we tune  
126 the model's parameters, evaluate the models using resampling, and subsequently, we run them on  
127 the testing dataset. Finally, we use the best-performing model to estimate and evaluate the daily  
128 spatial variation of  $\Psi_s$ .

## 129 2. Materials and Methods

### 130 2.1. Study Area



132 **Figure 1.** Study Area. The map on the left shows the orchards' location in Chile's central region. The maps on the right  
133 display the orchards in (a) Rio Claro and (b) La Esperanza, and (c) and (d) represent the irrigation treatments (T0, T1, T2, T3,  
134 T4). The red and blue dots represent the experimental trees selected for the 2022-2023 and 2023-2024 seasons,  
135 respectively, while the yellow dots indicate the trees selected for both seasons.

136 We conducted the study in two commercial orchards of sweet cherry trees (*Prunus avium* L., variety  
137 Regina) from the company Garces Fruit ([www.garcesfruit.com](http://www.garcesfruit.com)) in the O'Higgins region of central  
138 Chile. The orchards are *Rio Claro*, having 60 ha and 9 year-olds, and *La Esperanza*, with 40 ha and 6  
139 year-olds (Fig. 1a and 1b). The study took place during the irrigation seasons 2022–2023 and  
140 2023–2024, which run from October to April. In *Rio Claro*, the soil has a sandy loam texture with low  
141 moisture retention, whereas in *La Esperanza*, the field is located on clayey soil with high moisture  
142 retention. For the two orchards in both seasons, full bloom occurred in October. The harvest in *Rio*  
143 *Claro* was on December 23rd, 2022, and January 3rd, 2024, and in *La Esperanza* on December 12th,  
144 for both seasons.

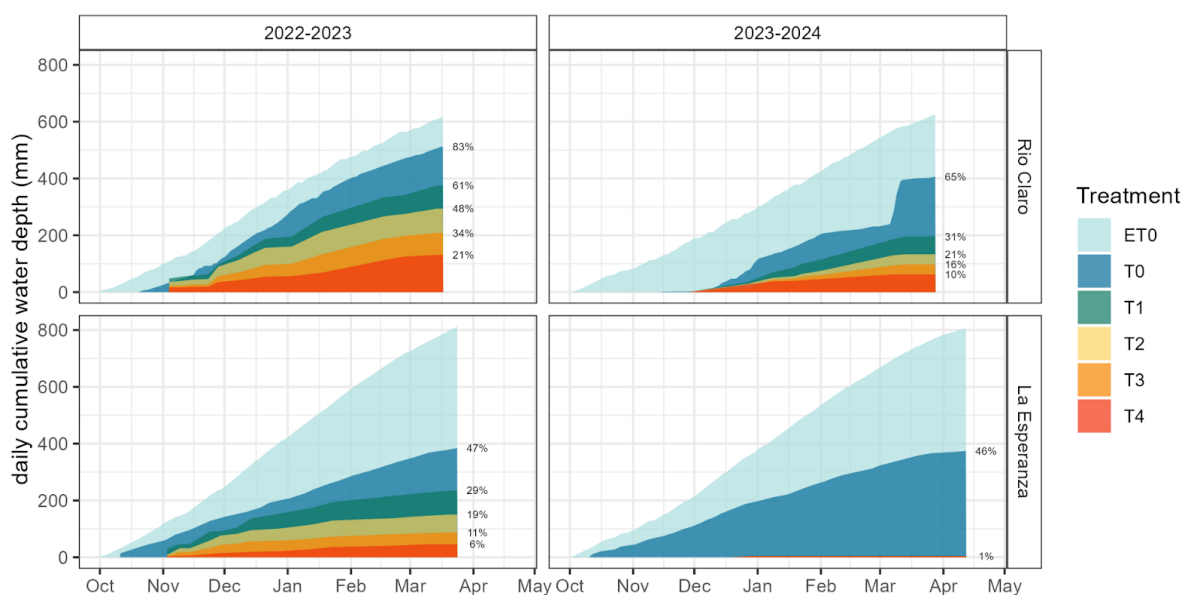
145 The climate of the region is mediterranean (Csb) (Beck et al., 2018) with moderate rainfall and an  
146 annual precipitation ranging from 200 to 500 mm year<sup>-1</sup> in the past 10 years, concentrated in winter,  
147 with a prolonged dry season of 7 to 8 months (DMC, 2024). Each orchard has a private weather  
148 station nearby, located 0.6 km from the center in *Rio Claro* and 1.4 km from the center in *La*  
149 *Esperanza*, respectively.

## 150 2.2. Deficit Irrigation

151 The local producer's irrigation in both orchards involves drip irrigation with two lines per row,  
 152 operating from October to April (spring–summer) and halting during the winter dormancy period. In  
 153 order to enhance the variability of plant water status, we implemented five different irrigation  
 154 repositioning treatments in each orchard. To manage the irrigation amount, we used the  $ET_0$  and  $\Psi_s$ ,  
 155 as references. Thus, we have T1, T2, T3, and T4 irrigation treatments, with T1 being the least  
 156 restrictive and T4 the most restrictive regarding water supply (Fig. 1c and 1d). We also have a  
 157 control treatment (T0) that receives standard irrigation from the local producer. Each treatment plot  
 158 contained 60 trees and covered 0.048 ha. We applied the treatments during the consecutive  
 159 growing seasons of 2022–2023 and 2023–2024. However, we did not irrigate treatments T1 to T4 in  
 160 *La Esperanza* during the second season, as the previous season's results did not demonstrate any  
 161 significant impact from the water restriction treatments. Table 1 shows the total volume of  
 162 reference water demand ( $ET_0$ ), the total volume of water applied by the local producer in the  
 163 control treatment (T0), and the total volume applied in deficit irrigation treatments, while Fig. 2  
 164 illustrates the cumulative water depth (mm) for each treatment during irrigation, and the  
 165 percentage relative to  $ET_0$ .

166 **Table 1.** Total volume of reference evapotranspiration ( $ET_0$ ) and the volume of water applied in treatments for each  
 167 orchard during the 2022–2023 and 2023–2024 seasons.

Treatment	Total volume of water ( $m^3 ha^{-1}$ )			
	Rio Claro		La Esperanza	
	2022-2023	2023-2024	2022-2023	2023-2024
$ET_0$	6,178	6,233	8,119	8,056
T0	5,128	4,066	3,840	3,740
T1	3,749	1,958	2,350	46
T2	2,937	1,333	1,504	25
T3	2,083	979	875	16
T4	1,312	625	456	46



168

169 **Figure 2.** Variation of daily cumulative water depth (mm) applied by irrigation per treatment in comparison with reference  
 170 evapotranspiration ( $ET_0$ ). The starting point for the accumulation of  $ET_0$  corresponds to the first day of irrigation for each  
 171 orchard and season.

## 172 **2.3. Data**

### 173 **2.3.1. In-situ midday stem water potential**

174  $\Psi_s$  was measured using a Scholander (Scholander et al., 1964) pressure chamber (Model 3000, Soil  
175 Moisture Equipment, Santa Barbara, CA, USA) connected to a nitrogen cylinder, following the  
176 procedures described by Turner (1981). Measurements were performed on mature leaves from the  
177 middle to the upper part of the tree on the north-facing side. We selected three trees per treatment  
178 in each orchard. One leaf per tree was sampled, totaling 15 measurements per orchard. In order to  
179 equilibrate the leaf water potential with the  $\Psi_s$ , leaves were wrapped in aluminum foil bags at least  
180 one hour before measurement. These measurements were conducted weekly between 12:00 and  
181 14:00 h during both seasons, resulting in total measurement counts of 412 for Rio Claro (212 for  
182 2022-2023; 200 for 2023-2024) and 486 for La Esperanza (176 for 2022-2023; 310 for 2023-2024).

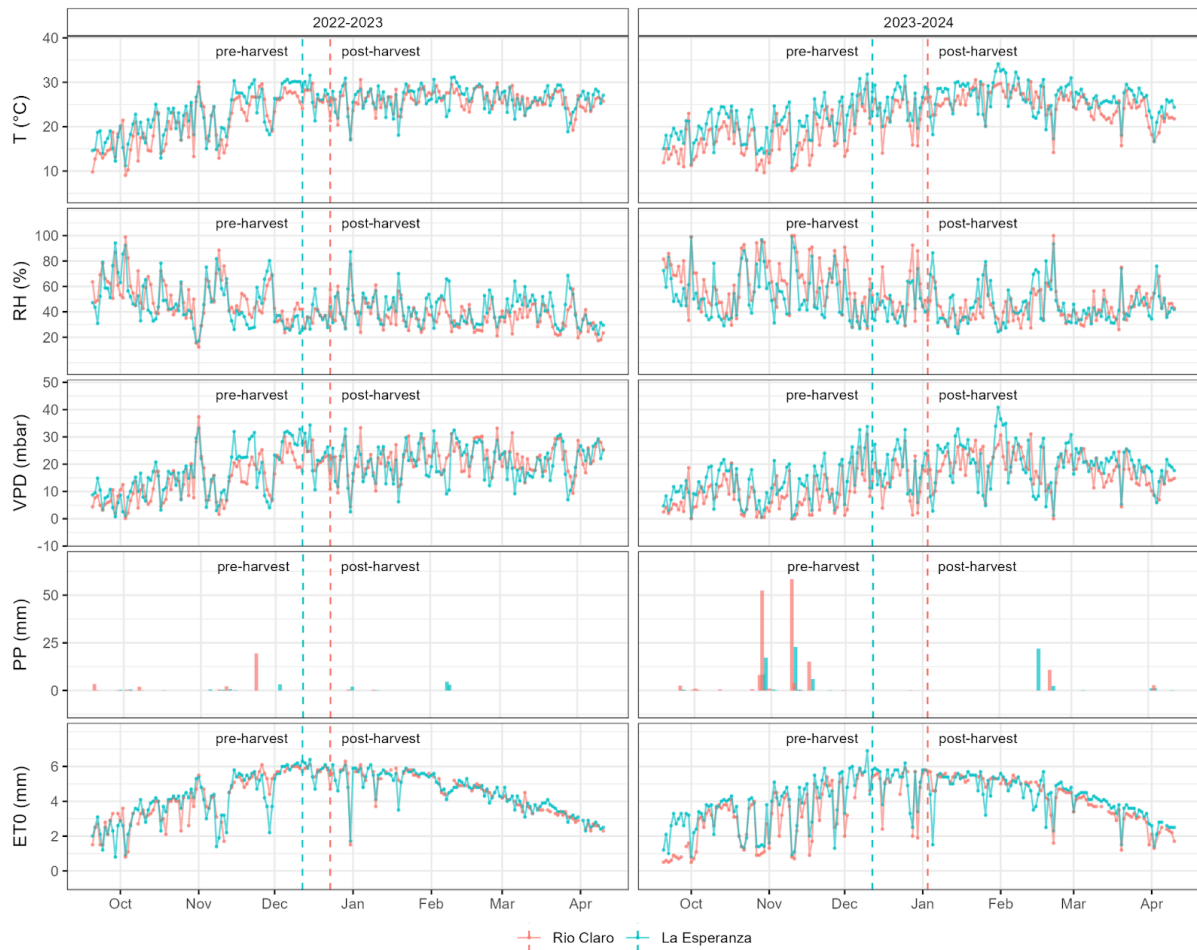
### 183 **2.3.2. Sentinel-2**

184 S2 mission consists of two identical satellites, S2A and S2B, both equipped with a multispectral  
185 sensor featuring 13 spectral bands covering visible, near-infrared, and shortwave infrared regions,  
186 with spatial resolutions of 10, 20, and 60m (see Table S2). In this study, we utilized a total of 106 S2  
187 (A/B) images, 54 for the 2022-2023 and 52 for the 2023-2024 season, captured between October  
188 and May in both orchards, tiles T19HCB for *La Esperanza* and T19HBB for *Río Claro*. The images were  
189 obtained from the atmospherically corrected S2 Level-2A collection from Planetary Computer  
190 (Microsoft Open Source et al., 2022), with a frequency of 5 days, at approximately 14:30 local time  
191 (UTC-4). A mask was applied based on the Scene Classification Layer (SCL) for values corresponding  
192 to “Cloud Shadows,” “Cloud Medium Probability,” and “Cloud High Probability,” respectively.

## 193 **2.4. Deriving spatio-temporal predictors**

### 194 **2.4.1. In-situ weather variables**

195 The automatic weather stations within both orchards recorded data on weather variables utilizing  
196 the ATMOS-41 model of METER group. These stations provided measurements of multiple  
197 meteorological variables every 15 minutes. We selected five meteorological variables that may  
198 affect water availability and plant physiological functionality: temperature ( $T^\circ$ ), relative humidity  
199 (RH), vapor pressure deficit (VPD), precipitation (PP), and reference evapotranspiration (ET0) (Fig. 3).  
200 We summed the precipitation and averaged the other variables daily.



201

202 **Figure 3.** Time series of weather variables at the orchard sites *Rio Claro* and *La Esperanza* and the seasons 2022-2023 and  
 203 2023-2024. Vertical dashed lines indicate the harvest date for each orchard and season.

#### 204 2.4.2. Vegetation indices derived from Sentinel-2

205 Sixteen VIs related to plant condition—vigor, stress, photosynthetic functionality, and water  
 206 content—were derived from S2 data, as shown in Table 2. Nine indices do not include red-edge  
 207 information, originating solely from the visible, NIR, and SWIR wavelength bands: NDVI, EVI, GCI,  
 208 NDWI, NBR, NDMI, MSI, NMDI and DWSI. In contrast, seven indices—CLr, Clg, NDRE1, NDRE2, NDCI,  
 209 mSR705, and RESI—were derived from red-edge information. The indices were calculated from the  
 210 preprocessed images of S2 bands, obtaining time series for each VI across both orchards and  
 211 seasons.

212 We applied a smoothing process using local polynomial regression (LOESS) (Cleveland, 1979) to  
 213 reconstruct the time series (e.g., masked cause of cloudiness) of VIs. The LOESS was implemented  
 214 with a smoothing parameter (span) set to 0.3. As a result, a smooth, continuous daily predicted  
 215 series for each index was obtained and then extracted for every measured tree. A correlation  
 216 analysis was performed to evaluate the relationship between these smooth series and the observed  
 217  $\Psi_s$  (see Fig. S2). The Pearson correlation coefficient ( $r$ ) was calculated across the trees for each day,  
 218 orchard and season, and only daily significant correlations ( $p$ -value < 0.05) were used to compute a  
 219 mean.

### 220 2.4.3. Biophysical parameters estimated from Sentinel-2

221 The Sentinel Application Platform (SNAP) is an integrated development environment (IDE) created  
 222 by the European Space Agency (ESA, 2024) for analyzing and processing satellite data. SNAP  
 223 provides a versatile suite of tools and functionalities for handling data from various Sentinel  
 224 missions, including a biophysical parameter algorithm. This algorithm consists of two key  
 225 components: (1) a radiative transfer model that inverts radiative properties from S2’s multispectral  
 226 imagery to retrieve vegetation parameters, and (2) a neural network model that further refines  
 227 these parameters using empirical data. By applying these models and empirical relationships, SNAP  
 228 extracts detailed information about the vegetation’s physiological status (Weiss et al., 2020).

229 Using SNAP, we calculated various biophysical parameters, including LAI—leaf area index;  
 230 FAPAR—fraction of absorbed photosynthetically active radiation; FVC—fraction of vegetation cover;  
 231 CCC—canopy chlorophyll content; and CWC—canopy water content. These parameters were  
 232 processed at 20 m for both seasons and orchard sites, and the same smoothing process used for  
 233 reconstructing the time series of VIs was applied. The resulting biophysical parameters were used as  
 234 predictors for modeling  $\Psi_s$ , along with the VIs and weather data (Table 2).

235 **Table 2.** Predictor variables for  $\Psi_s$  modeling. Weather variables from automatic stations (15 min frequency): T (°C), RH (%),  
 236 VPD (mbar), PP (mm), ET0 (mm). Vegetation indices (VIs) derived from Sentinel-2 bands (10 m resolution) and biophysical  
 237 parameters from SNAP (20 m resolution), both at 5-day intervals. B2 to B12 refer to Sentinel-2 MSI band reflectance.

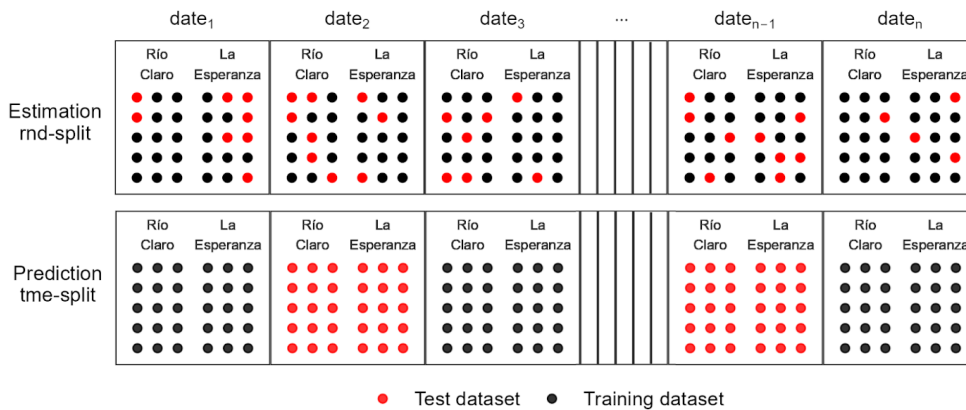
Classification	Name	Description	Algorithm/Formula	Reference
Weather variables	T	Temperature		
	RH	Relative Humidity		
	VPD	Vapor Pressure Deficit	$e^s - e^a$	Allen et al. (1998)
	PP	Precipitation		
	ET0	Reference Evapotranspiration	FAO-Penman-Monteith	Allen et al. (1998)
Vegetation indices	NDVI	Normalized Difference Vegetation Index	$\frac{B8 - B4}{B8 + B4}$	Rouse et al. (1974)
	EVI	Enhanced Vegetation index	$\frac{2.5 \cdot (B8 - B4)}{(B8 + 6 \cdot B4 - 7.5 \cdot B2 + 1)}$	Huete et al. (2002)
	GCI	Green Coverage Index	$\frac{B9}{B3} - 1$	Gitelson et al. (2003)
	NBR	Normalized Burn Ratio	$\frac{B8 - B12}{B8 + B12}$	García and Caselles (1991)
	NDWI	Normalized Difference Water Index	$\frac{B3 - B8}{B3 + B8}$	McFeeters (1996)
	NDMI	Normalized Difference Moisture Index	$\frac{B8 - B11}{B8 + B11}$	Gao (1996)
	MSI	Moisture Stress Index	$\frac{B11}{B8}$	Huntjr and Rock (1989)
	NMDI	Normalized Multi-band Drought Index	$\frac{B8 - (B11 - B12)}{B8 + (B11 - B12)}$	Wang and Qu (2007)
	DWSI	Disease and Water Stress Index	$\frac{B8 + B3}{B11 + B4}$	Apan et al. (2004)
	Clr	Red Edge Chlorophyll	$\frac{B7}{B5} - 1$	Gitelson et al. (2003)
	Clg	Green Chlorophyll Index	$\frac{B7}{B3} - 1$	
	NDRE1	Normal Deviation Index of the Red Edge 1	$\frac{B6 - B5}{B6 + B5}$	Sims and Gamon (2002)
	NDRE2	Normal Deviation Index of the Red Edge 2	$\frac{B8 - B5}{B8 + B5}$	Barnes et al. (2000)
	NDCI	Normalized Difference Chlorophyll Index	$\frac{B5 - B4}{B5 + B4}$	Mishra and Mishra (2012)
	mSR705	Red Edge modified Simple Ratio	$\frac{(B6/B5) - 1}{\sqrt{(B6/B5) + 1}}$	Wu et al. (2008)
RESI	Red Edge Spectral Index	$\frac{B7 + B6 - B5}{B7 + B6 + B5}$	Xiao et al. (2020)	

Classification	Name	Description	Algorithm/Formula	Reference
Biophysical parameters	LAI	Leaf Area Index	PROSPECT + SAIL coupled model	Marie Weiss et al. (2020) Baret and Buis (2008)
	fAPAR	Fraction of Absorbed Photosynthetically Active Radiation		
	FVC	Fraction of Vegetation Cover		
	CCC	Canopy Chlorophyll Content		
	CWC	Canopy Water Content		

## 238 2.6. Modeling the daily spatial $\Psi_s$

### 239 2.6.1. Machine learning models (ML)

240 For  $\Psi_s$  modeling, we tested three machine learning algorithms (ML) : 1) Extreme Gradient Boosting  
241 (XGBoost; Chen and Guestrin, 2016); 2) Random Forest (RF; Ho, 1995); and 3) Support Vector  
242 Machine (SVM; Cortes and Vapnik, 1995). The first two methods utilize decision trees, while the  
243 latter employs support vectors. We selected these models because they are state-of-the-art, require  
244 few training samples (compared to neural networks), and are interpretable. These ML algorithms  
245 can be used for both classification and regression. We carried out a regression analysis, using the  $\Psi_s$   
246 as the outcome and using 26 predictors: five of weather, 16 VIs, and five biophysical parameters  
247 (Table 2). We used 26 dates from seasons 2022–2023 and 34 from 2023–2024, totaling 60 dates. For  
248 each date, we take 30 measurements, 15 per orchard (*Río Claro* and *La Esperanza*). Thus, the  
249 complete dataset has 883 observations. For the modeling process, we proceed as follows: i) prepare  
250 and split the dataset into training and testing; ii) use the training dataset to adjust the algorithms'  
251 parameters by hyperparameter optimization; iii) resampling to account for reliability and recognize  
252 the most relevant variables to estimate  $\Psi_s$ , and iv) evaluate the model to gather the performance.



253

254 **Figure 4.** Split schemes used for grouping in training and testing datasets for the random split (*rnd\_split*) and the  
255 independent time split (*ind\_split*).

256 We trained the three models using two splitting schemes (Fig. 4), one in which we considered a  
257 random split taking testing and training data randomly (*rnd\_split*) and a second one in which we  
258 used independent dates for training and testing (*tme\_split*). We chose 75% of the data for training  
259 and 25% for testing in both cases. We used three types of feature engineering on the training data:  
260 i) we removed the predictors whose values remain constant by removing the zero-variance  
261 variables; ii) we normalized the predictors as they have a mean of zero and a standard deviation of  
262 one; and iii) we tested a model version that used partial least squares (PLS) (Wold, 1966) to cut  
263 down on the number of dimensions and used the five principal components as predictors. As a

264 result, we used models with normalized predictors and others with the five principal components  
 265 estimated by PLS.

266 To adjust the parameters of the models (XGBoost, RF, SVM) we used hyperparameter optimization.  
 267 We start by setting each parameter's range (Table 3). We used five folds for resampling for both  
 268 splitting schemes (*rnd\_split* and *tme\_split*). The hyperparameter optimization used a set of ten  
 269 combinations of parameters per model. To evaluate the performance of the models, we used the  
 270 metrics  $R^2$ , root-mean-square error (RMSE), and mean absolute error (MAE). Finally, we ranked the  
 271 models based on the RMSE and  $R^2$ , selecting the models with the lowest RMSE and higher  $R^2$ .

272

273 **Table 3.** Range of initial values for the parameters adjusted in the tuning process for the models Extreme Gradient Boosting  
 274 (XGBoost), Random Forest (RF), and Support Vector Machines (SVM).

Model	Parameter description	Identifier	Range
XGBoost and Random Forest	The number of trees contained in a random forest or boosted ensemble	trees	1000
	Number of randomly sampled predictors	mtry	1 - 28
	The minimum number of data points in a node that is required for the node to be split further	n_min	2 - 40
XGBoost	The maximum depth of the tree	tree_depth	1 - 15
	Learning rate	learn_rate	-3 - -0.5
	The reduction in the loss function required to split further	gamma	-10 - 1.5
	The size of the data set used for modeling within an iteration of the modeling algorithm	sample_size	0.1 - 1
Support Vector Machines	Regularization parameter	cost	-10 - 5
	Radial basis function sigma	rbf_sigma	-10 - 0

275

### 276 2.6.3. Evaluation and variable importance for the models

277 To evaluate the performance of the models, we used resampling over the training dataset for both  
 278 splitting schemes (*rnd\_split* and *tme\_split*). We selected five folds, and calculated the metrics  $R^2$ ,  
 279 MAE, and RMSE for each fold.

280 To estimate the variable importance of each predictor on the model's performance, RF employs an  
 281 out-of-bag permutation method in each tree, permuting over the predictors, and calculates the  
 282 mean-square-error for each instance. For XGBoost, we estimate the fractional contribution of each  
 283 feature to the model based on the total gain of the corresponding feature's splits. In the case of  
 284 SVM, we compute permutation-based variable importance scores for the predictors (for more  
 285 detail, see Greenwell and Boehmke, 2020).

### 286 2.7. Spatio-temporal variation of estimated $\Psi_s$

287 To estimate the daily spatial variation in the orchards of *Rio Claro* and *La Esperanza*, we selected the  
 288 best-performing model from those generated with the random split (*rnd\_split*). This was done for all  
 289 the days within each season. To analyze the spatial variation, we identified the days with the highest  
 290 coefficient of variation. To assess the temporal variation we averaged the  $\Psi_s$  within each irrigation

291 treatment and compared the difference between them for the two seasons. Also, using boxplot  
292 graphs, we compared the monthly distribution of values of  $\Psi_s$  for the five treatments.

## 293 **2.8. Software**

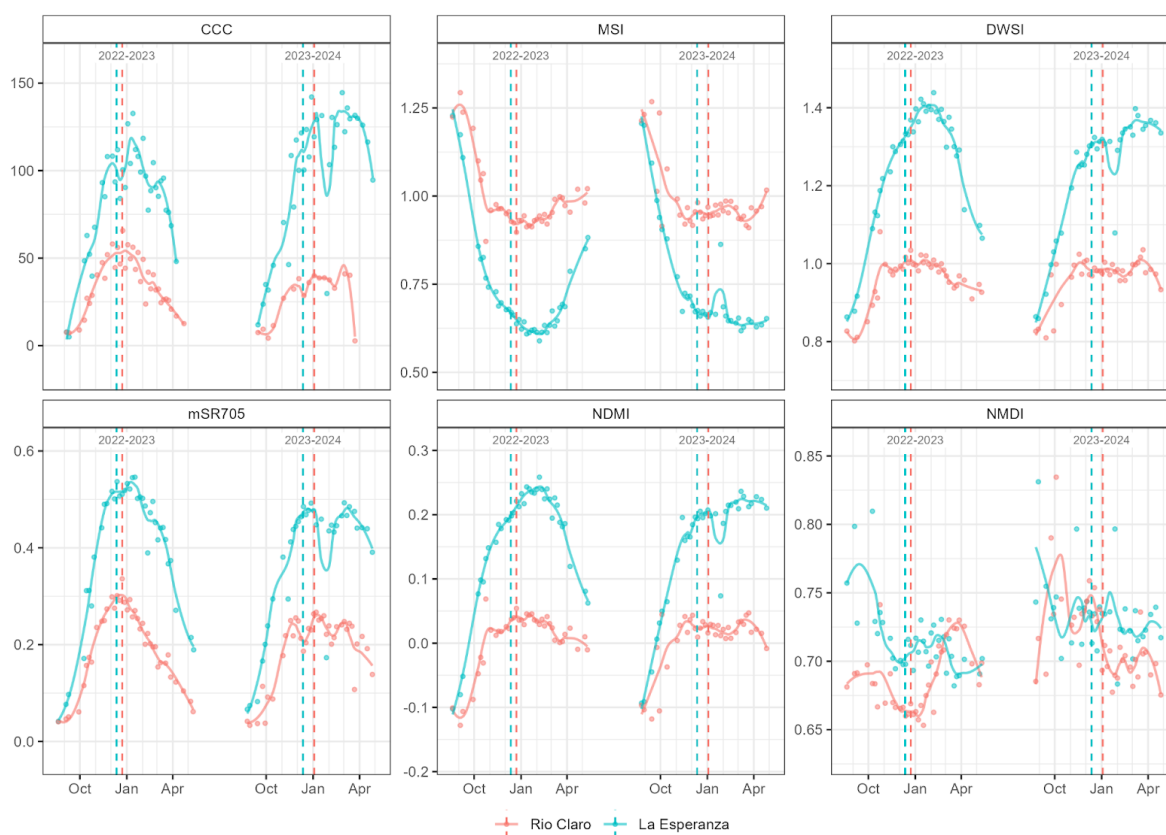
294 For downloading, processing, analyzing spatio-temporal data, and machine learning modeling, we  
295 used the R programming language for statistical computing and graphics (R Core Team, 2022). We  
296 used the data available in Planetary Computer (Microsoft Open Source et al., 2022), which we  
297 accessed via the {rstac} package (Simoes et al., 2021). Preprocessing tasks, such as applying cloud  
298 coverage masks and cropping to the orchard plots, were performed using {gdalcubes} (Appel et al.,  
299 2021). For processing raster data, we used {terra} (Hijmans, 2024). To manage vectorial data, we  
300 used {sf} (Pebesma, 2018). For mapping, we used {tmap} (Tennekes, 2018). For data analysis and  
301 visualization, the suite {tidyverse} (Wickham et al., 2019) was used. For the machine learning  
302 modeling, we used the {tidymodels} (Kuhn and Wickham, 2020), {workflowsets} (Kuhn and Couch,  
303 2024), {recipes} (Kuhn et al., 2024), {ranger} (Wright and Ziegler, 2017), {xgboost} (Chen et al., 2024),  
304 and {kernlab} (Karatzoglou et al., 2004) packages.

## 305 **4. Results**

### 306 **4.1. Predictors and their relation to $\Psi_s$**

#### 307 **4.1.2. Smoothing of Sentinel-2 derived indicators**

308 Fig. 5 shows the raw and smoothed-interpolated values of the most important satellite indicators in  
309 the model's performance for a representative tree across both seasons and orchard sites. The values  
310 of the indices indicate variations in behavior throughout the various growing seasons. In both  
311 orchards, CCC, DWSI, mSR705, and NDMI increase during leaf expansion and higher water demand  
312 months (summer), peaking around or shortly after harvest dates between Jan-Mar and decreasing  
313 with leaf loss in Mar-Apr. In contrast, MSI exhibits opposite seasonal variability, reaching its lowest  
314 point after the harvest dates. NMDI shows unique behavior, with a tendency to decrease in the  
315 summer but with variable peaks throughout most months. The resulting series reveals a difference  
316 in magnitudes between the two orchards, with *La Esperanza* exhibiting higher values compared to  
317 *Rio Claro*, except for MSI, in which the behavior is opposite. Regarding both seasons, there are  
318 similarities in magnitude and variability, except for a sudden peak in *La Esperanza* during the second  
319 season between Jan-Mar and for NMDI in general.



320

321 **Figure 5.** Time series of raw and smoothed-interpolated Sentinel-2 derived indicators most important to the model's  
 322 performance at both orchard sites and seasons. Red points and lines correspond to Río Claro, while blue represents La  
 323 Esperanza. Vertical dashed lines indicate the harvest dates for each orchard and season.

### 324 4.1.3. Correlation between predictors and $\Psi_s$

325 Table 4 presents the Pearson correlation coefficients between the daily mean values of each  
 326 weather variable and the observed daily mean  $\Psi_s$ . The results indicate that ET0, VPD, and T are  
 327 negatively correlated with  $\Psi_s$ , while RH shows a positive correlation, and PP only exhibits weak  
 328 correlations ranging between 0.1 and -0.1 for both sites during the 2022-2023 season. ET0  
 329 demonstrates a strong correlation ( $r \leq -0.7$ ) at *La Esperanza* in both seasons, but not at *Río Claro*. In  
 330 contrast, VPD, T, and RH generally exhibit strong correlations in most cases.

331 **Table 4.** Pearson correlation coefficient ( $r$ ) between daily weather data and daily observed  $\Psi_s$  (MPa).

Variable	Pearson correlation coefficient ( $r$ )			
	Río Claro		La Esperanza	
	2022-2023	2023-2024	2022-2023	2023-2024
ET0	-0.38	0	-0.77	-0.86
VPD	-0.75	-0.39	-0.66	-0.89
T	-0.8	-0.45	-0.81	-0.88
RH	0.75	0.43	0.53	0.83
PP	0.11		-0.1	

332 Regarding S2 derived predictors, Table 5 presents the mean of daily significant Pearson correlation  
 333 coefficients ( $r$ ;  $p \leq 0.05$ ) between these predictors and the observed  $\Psi_s$  (MPa) for the 15 trees at  
 334 both orchard sites and seasons. The results reflect differences between indices with positive and  
 335 negative correlations, consistent with the seasonal behavior of these shown in Fig. 5. For CCC, DWSI,

336 mSR705, and NDMI, the mean correlations were positive and moderate ( $\geq 0.5$ ) in all cases except  
 337 for *La Esperanza* season 2023-2024, where CCC exhibited both positive and negative correlations on  
 338 different days (Table 5). The same situation occurs with NMDI, which, along with MSI, averaged  
 339 negative and moderate correlations ( $\leq -0.5$ ) in all cases except for this specific group, where NMDI  
 340 showed a positive correlation. Regarding the seasons, more significant correlations were found in  
 341 the first season than in the second. In terms of orchards, more significant correlations were  
 342 observed in *Río Claro* compared to *La Esperanza*.

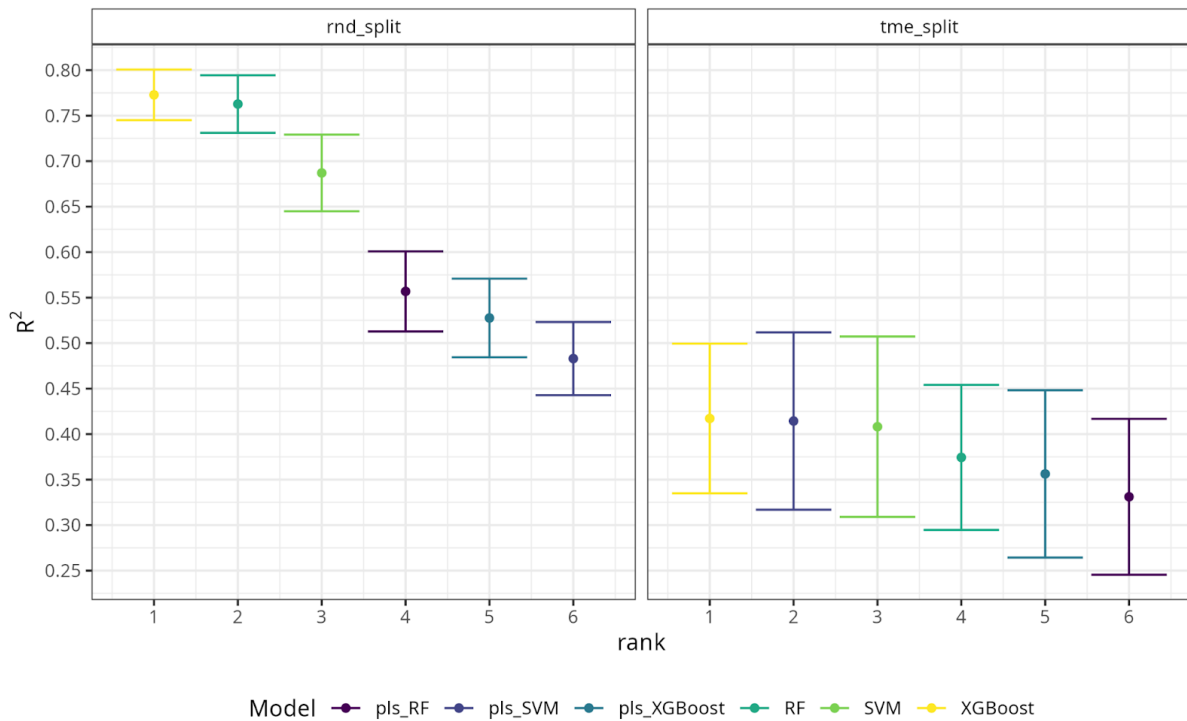
343 **Table 5.** Mean of daily significant Pearson correlation coefficients ( $r$ ) between Sentinel-2 derived predictors and observed  
 344  $\Psi_s$  (MPa) for the 15 trees across both orchard sites and seasons.  $n$  denotes the number of daily significant  $r$  obtained.

Orchard site	Season	Variable	$r \pm sd$	$n$
Río Claro	2022-2023	CCC	$0.69 \pm 0.11$	5
		MSI	$-0.66 \pm 0.13$	5
		DWSI	$0.65 \pm 0.12$	4
		mSR705	$0.69 \pm 0.13$	9
		NDMI	$0.66 \pm 0.13$	5
		NMDI	$-0.69 \pm 0.1$	6
	2023-2024	CCC	$0.66 \pm 0.01$	2
		mSR705	$0.63 \pm 0.04$	2
		NMDI	-0.55	1
La Esperanza	2022-2023	MSI	-0.59	1
		DWSI	0.61	1
		mSR705	0.52	1
		NDMI	0.59	1
	2023-2024	CCC*	$0.03^* \pm 0.88$	2*
		NMDI	0.54	1

### 345 4.3. Modeling the daily spatial $\Psi_s$

#### 346 4.3.1. Evaluation and variable importance of the models

347 Fig. 6 displays the  $R^2$  ranking for each of the twelve different models trained with resampling (three  
 348 algorithms, two splittings, and with or without partial least squares). Using the RMSE metric, the  
 349 ranking behaves equally. With *rnd\_split*, the  $R^2$  range is 0.45 to 0.8, and with *tme\_split*, it decreases  
 350 to a range of 0.25 to 0.52. In the case of *rnd\_split*, XGBoost and RF reached the highest  $R^2$  with a  
 351 mean of 0.77 and 0.76, respectively, followed by SVM with a  $R^2$  of 0.68. On the *tme\_split*, the  $R^2$   
 352 difference between models is minor in comparison to those trained on the *rnd\_split*. The three  
 353 models that reached the maximum  $R^2$  on *tme\_split* are XGBoost, pls\_SVM (trained with the five  
 354 principal components obtained from the partial least squares analysis as predictors), and SVM,  
 355 which are around 0.45. We selected the three models that reached the highest performance in the  
 356 resampling evaluation per splitting scheme, hereafter named RF, XGBoost, and SVM.



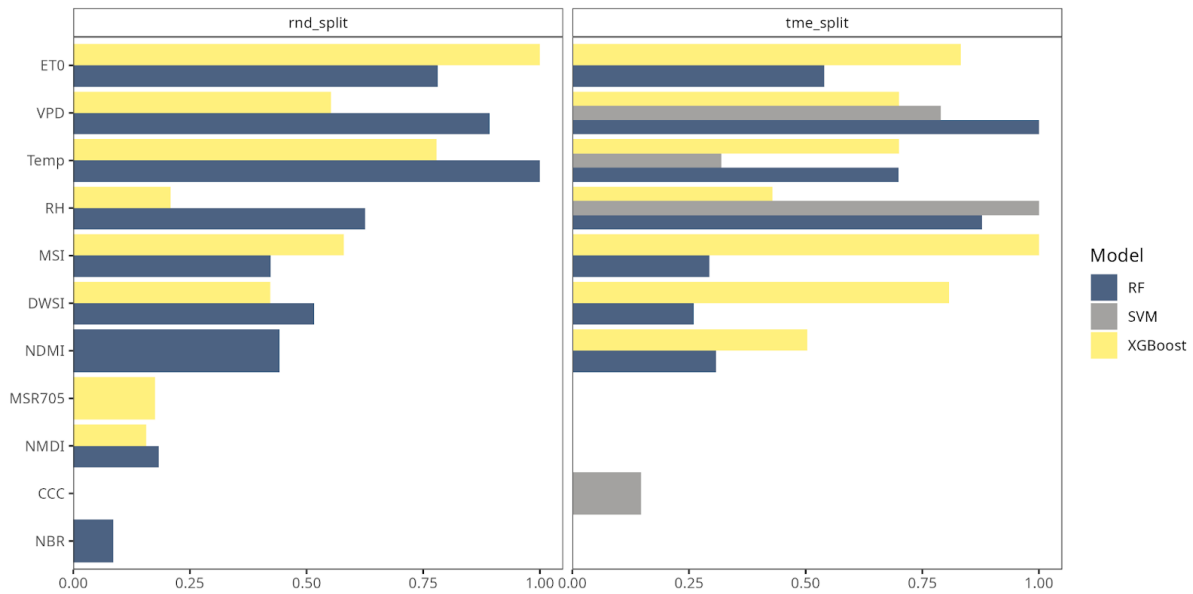
357

358 **Figure 6.** Ranking of machine learning models in the resampling according to the  $R^2$  metric. The models are Random forest  
 359 (RF), extreme gradient boosting (XGBoost), and support vector machines (SVM). The "pls" acronym beside the model name  
 360 stands for partial least squares. Each panel corresponds to a splitting scheme: a random split (*rnd\_split*) and a  
 361 time-independent split (*tme\_split*).

362

363 Fig. 7 shows the eleven most important variables in the model's performance. In the two splitting  
 364 schemes, the meteorological data, specifically ET0, VPD, and temperature, hold the highest  
 365 importance and reach their maximum weight. In SVM, RH is the only predictor in the *rnd\_split*, and  
 366 RH, VPD, and temperature are the predictors with higher importance in the *tme\_split*. The  
 367 S2-derived predictors came in second place after meteorological data. In the *rnd\_split*, MSI, DWSI,  
 368 mSR705, NDMI, and NMDI are the most relevant predictors for RF and XGBoost. When considering  
 369 the *tme\_split*, the MSI, DWSI, and NDMI are the most contributing variables to the model's  
 370 performance. In the case of the SVM model for *tme\_split*, the biophysical parameter CCC holds the  
 371 highest importance. As expected, the S2 predictors that were more closely related to  $\Psi_s$  were those  
 372 using the SWIR wavelength, which is the spectral region more sensitive to water.

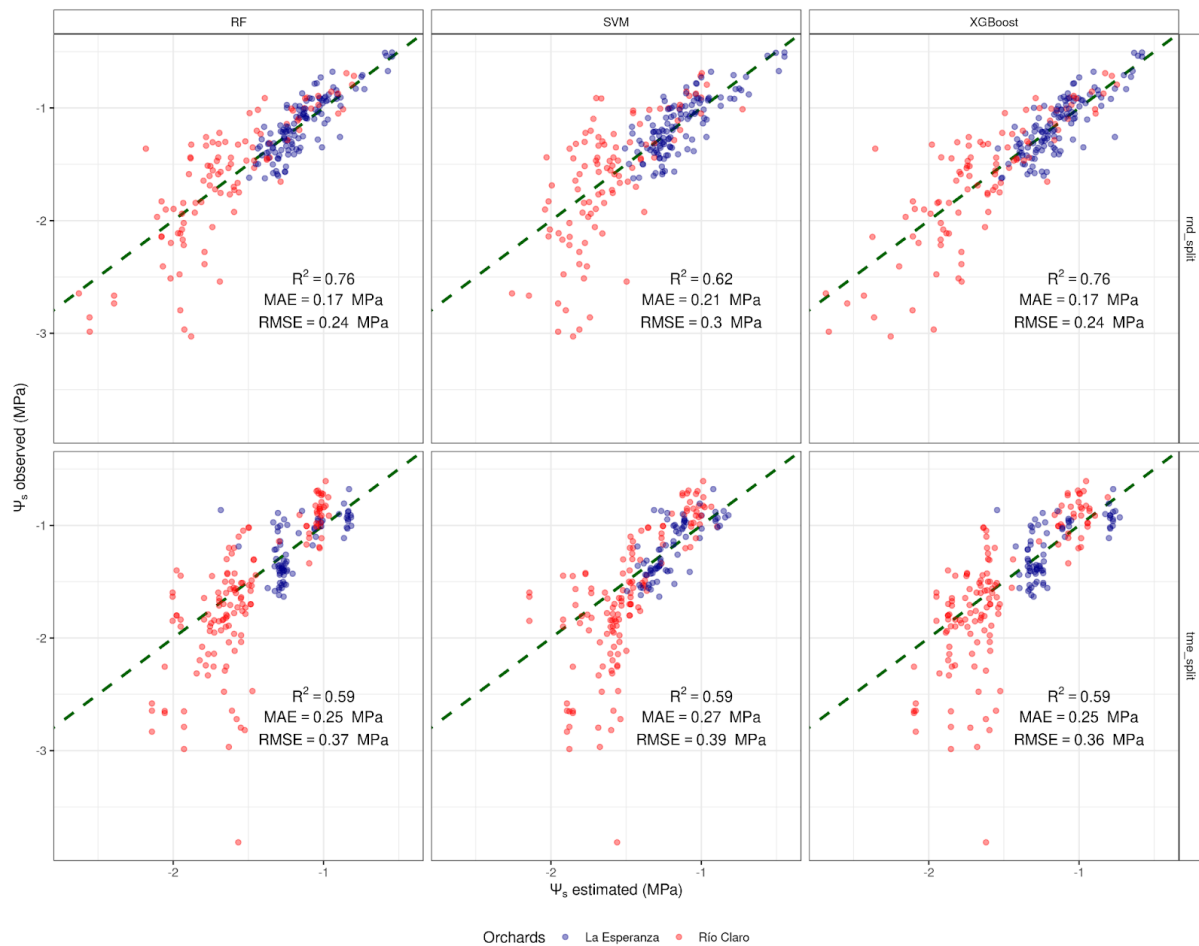
373



374

375 **Figure 7.** Scaled variable importance (0–1) per machine learning models: random forest (RF), extreme gradient boosting  
 376 (XGBoost), and support vector machines (SVM); for the two splitting schemes: random split (*rnd\_split*) and time  
 377 independent split (*tme\_split*).

378 After the resampling evaluation, we trained the models on the testing dataset. In the *rnd\_split*, the  
 379  $R^2$  was 0.76, 0.76, and 0.62 for XGBoost, RF, and SVM, respectively (Fig. 8). The RMSE was between  
 380 0.24 MPa (XGBoost and RF) and 0.3 MPa (SVM). In the *rnd\_split*, RF and XGBoost improve  
 381 significantly over SVM. When trained in the *tme\_split*, the model's performance decreases in  
 382 comparison to those trained with *rnd\_split*. Between them the models behave equally, with an  $R^2$  of  
 383 0.59 for the three models. The RMSE was found to be between 0.36 MPa for XGBoost and 0.39 MPa  
 384 for SVM. In Fig. 8, it can be seen that the error (observed minus estimated) increases for values  
 385 lower than -1.5 MPa, corresponding to fewer points. Thus, the models do not have enough data to  
 386 allow them to increase their performance. The reason for the fewer data in this range is that it  
 387 corresponds to higher water stress levels. Critical stress can lead to plant stomatal closure, which  
 388 can impact both production and quality.



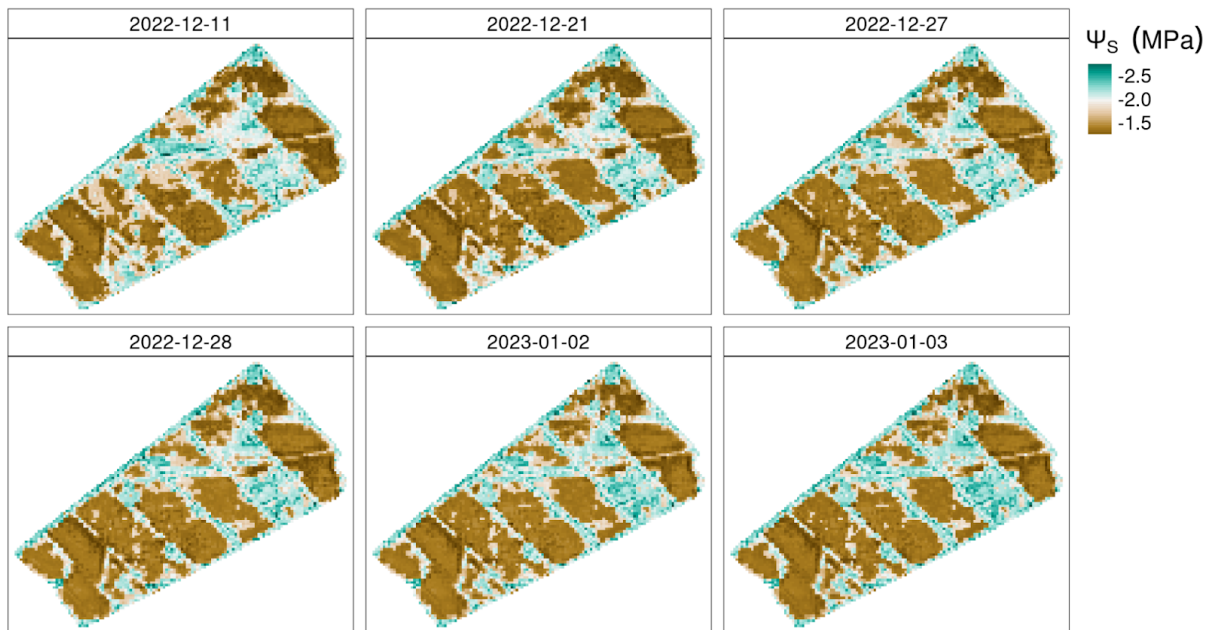
389

390 **Figure 8.** Predicted values into the testing dataset versus observed values of stem water potential ( $\Psi_s$ ) for La  
 391 Esperanza and Río Claro orchards. The vertical panels correspond to the machine learning model: random  
 392 forest (RF), extreme gradient boosting (XGBoost), and support vector machines (SVM). The horizontal panels  
 393 correspond to the splitting schemes: random split (*rnd\_split*) and time-independent split (*tme\_split*). The metrics  
 394 of performance used are r-squared ( $R^2$ ), mean absolute error (MAE), and root mean squared error (RMSE).

#### 395 4.4. Spatio-temporal variation of estimated $\Psi_s$

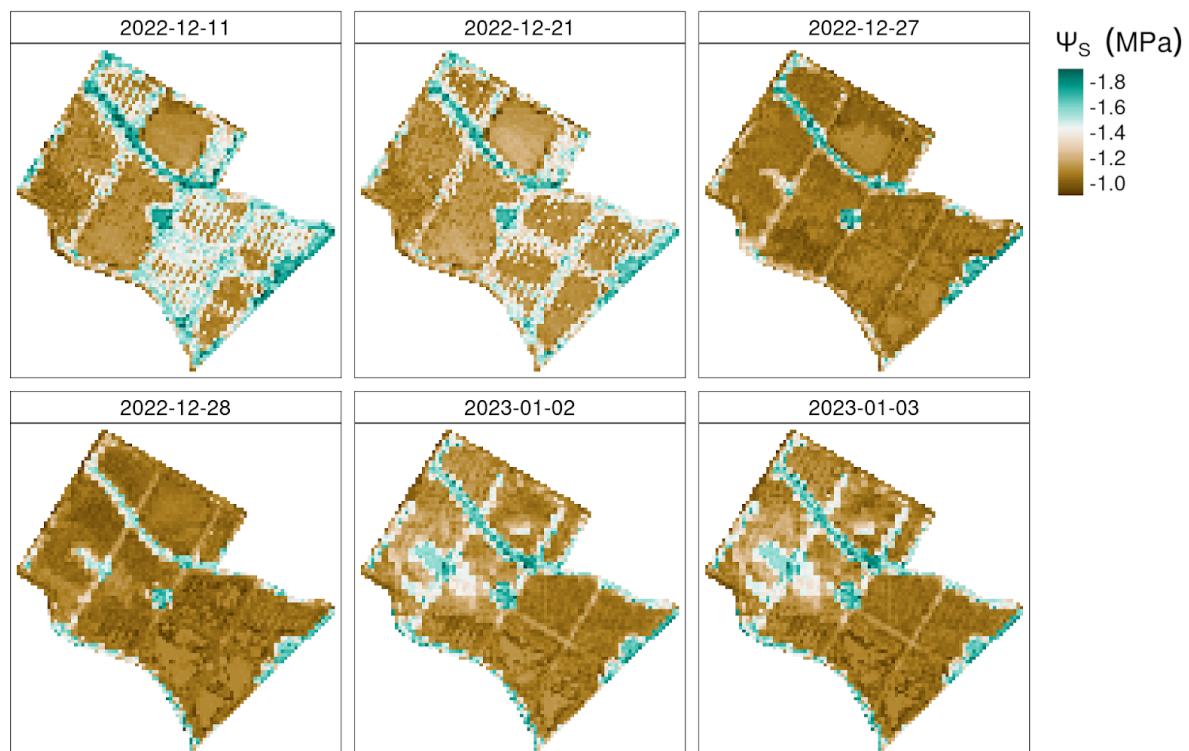
396 We used the XGBoost model trained over the *rnd\_tme* (best-performing model) to estimate the  
 397 daily spatial variation of  $\Psi_s$  over the orchard sites. Figs. 9 and 10 show the spatial variation of  $\Psi_s$  for  
 398 the six dates that had the highest spatial variation (i.e., coefficient of variation) for the two orchard  
 399 sites. The major spatial variation occurred in December and early January, corresponding to the  
 400 higher water demand months (summer). The estimation of the whole orchard includes roads and  
 401 infrastructure (see Fig. 1), which the model detects as the ones with lower  $\Psi_s$ . Despite that, the  
 402 spatial estimation allows us to identify sectors with different plant water statuses. Figs. 9 and 10  
 403 show that in the Río Claro orchard there is a higher spatial variation in comparison with La  
 404 Esperanza. In Río Claro, from the center to the north-east, a sector persists with lower pressures  
 405 below -2 MPa. In La Esperanza, the response of  $\Psi_s$  is more uniform, with December 11th showing  
 406 major spatial variation. However, given that this date coincides with harvest days, other factors such  
 407 as the presence of people in the area could potentially influence the variation.

408



409

410 **Figure 9.** Midday stem water potential ( $\Psi_s$ ) estimated by the extreme gradient boosting (XGBoost) model over the Río  
 411 Claro orchard. The days selected correspond to the six with the maximum coefficient of variation.



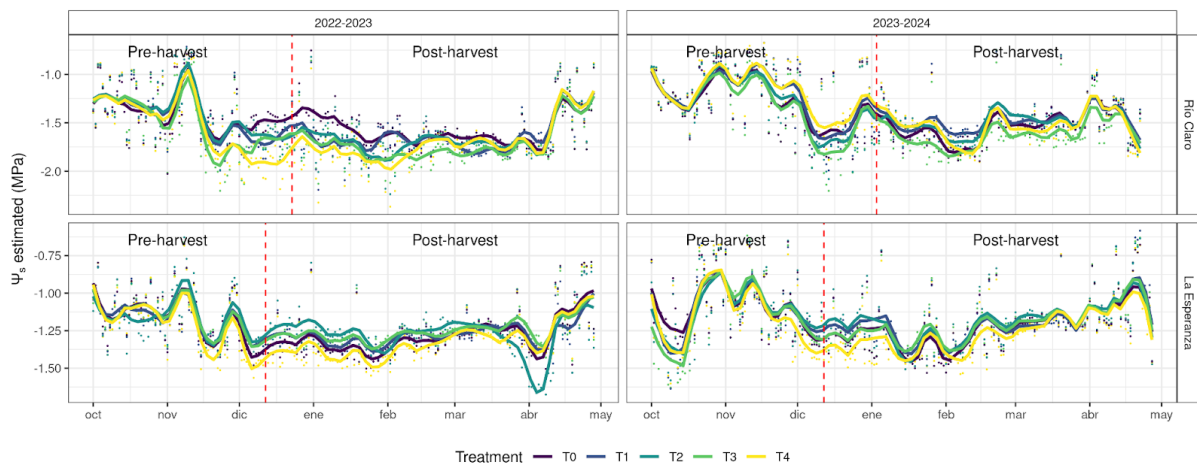
412

413 **Figure 10.** Midday stem water potential ( $\Psi_s$ ) estimated by the extreme gradient boosting (XGBoost) model over the La  
 414 Esperanza orchard. The days selected correspond to the six with the maximum coefficient of variation.

415

416 The averaged values of  $\Psi_s$  per treatment shown in Fig. 11 allow us to observe the temporal variation  
 417 of the plant water status through the irrigation season (October to April) and the difference  
 418 between treatments. The  $\Psi_s$  has been decreasing since October, reaching its lowest values between  
 419 December and February, and then increasing until April, in line with the plant's water demand. For  
 420 the two sites, the differences are most evident during the season 2022-2023 (Fig. 12), especially  
 421 from December to February. For 2023–2024, during November–December, the  $\Psi_s$  is higher in

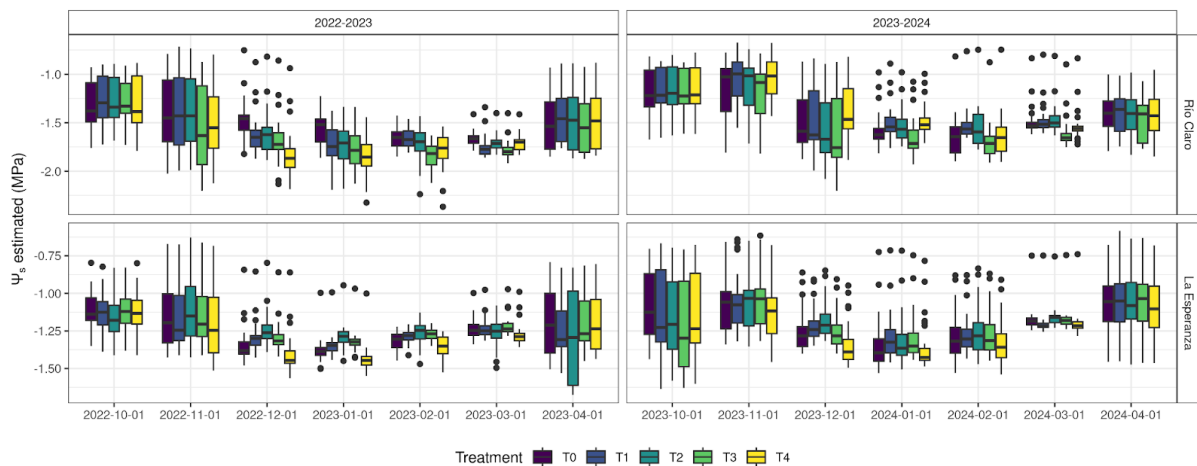
422 comparison to the previous season, this could be due to the precipitation fall during those months.  
 423 The dispersion of values of  $\Psi_s$  is higher for October, November, and April, and it is tighter for the  
 424 summer months (December–February) (Fig. 12). Additionally, the disparity between the various  
 425 irrigation levels is more pronounced for the years 2022–2023, with a noticeable decrease in  $\Psi_s$  from  
 426 T0 to T4, particularly in November and December. This could be attributed to the harsher climatic  
 427 conditions during the first season, which included higher temperatures and less precipitation,  
 428 leading to increased stress on the orchards.



429

430 **Figure 11.** Averaged values of stem water potential ( $\Psi_s$ ) estimated by the extreme gradient boosting model (XGBoost). The  
 431 lines are the smoothed series for the five irrigation treatments, the seasons 2022-2023 and 2023-2024, as well as the  
 432 orchards of Río Claro and La Esperanza.

433



434

435 **Figure 12.** Distribution of daily values of estimated stem water potential ( $\Psi_s$ ) by the extreme gradient boosting model  
 436 (XGBoost) per month within the irrigation treatments for the seasons 2022-2023 and 2023-2024, as well as the orchards  
 437 Río Claro and La Esperanza.

438

## 439 5. Discussion

### 440 5.1. Sources of uncertainty in the models

441 Some of the major sources of error in the model's prediction are the spatial resolution of the S2  
 442 images (10/20 meters), the temporal reconstruction of the time series of vegetation predictors, and,

443 to a lesser extent, the null spatial representation of the weather data. The satellite passes over the  
444 orchards near the time of the measurements, allowing for timely capture of the plant water status.  
445 However, one S2 pixel covers approximately 12 trees. Then, the cover area takes into account cherry  
446 canopy as well as background soil. Thus, the reflectance retrieved per pixel is a mixture of canopy  
447 and soil. This problem could be faced by spatial fusion techniques of S2 with high-resolution images  
448 (Dong et al., 2023; Galar et al., 2020) which will diminish the error due to this issue. Further, we  
449 used a simple low pass filter to interpolate daily values of vegetation predictors, which is a  
450 technique usually used for gap-filling in cloudy days (Mo et al., 2023), but not for interpolation.  
451 When assessing vegetation development, this technique may prove more beneficial as the  
452 physiological changes in development span more than a single day. However, the plant's water  
453 status changes on an hourly basis. A better approach to estimating daily values is the  
454 spatio-temporal fusion with Sentinel-3 (Wang and Atkinson, 2018) which takes into account the  
455 spectral reflectance. However, in this instance, a machine learning model that utilizes all predictors  
456 gathers temporal variation from weather data and spatial variability from S2 predictors. Therefore,  
457 the model operates effectively when the interpolated S2 predictors sustain the spatial variation  
458 related to plant water status. We test a different model that uses original spectral vegetation indices  
459 as predictors and only fill gaps on cloudy dates, but the results decrease significantly for the  
460 tme\_split (Figs. S4 and S5).

461 Because we have fewer measurements in the range of -1.75 to -2.5 MPa, our model performs poorly  
462 for lower values of SWP. To increase the performance of the model, future studies should consider  
463 collecting more points in this range. Other research that wasn't included in this article shows that  
464 for this species, the turgor loss point, or the point at which the plant stomatal closure happens, is  
465 less than -2 MPa. Therefore, if we intend to utilize this model for irrigation optimization, we must  
466 accurately estimate the SWP within this range.

467 Another source of uncertainty is regarding the values of SWP on cloudy days. In this study, we only  
468 take measurements on clear days. However, we use the LOESS to reconstruct the time series of  
469 spectral vegetation indices. Thus, in future work we need to consider taking measurements on  
470 cloudy days to evaluate the performance of the model on those days.

## 471 **5.2. Sentinel-2 predictors most related to $\Psi_s$**

472 The resulting S2 derived indices used as predictors for the model can be categorized based on their  
473 behavior between November and February, which corresponds to the period of rising temperatures,  
474 peak vegetative growth, and leaf expansion in cherry trees. Among the most significant of those  
475 affecting the model's performance, were DWSI, mSR705, and NDMI increasing during this period.  
476 Except for DWSI, these indices positively correlate with LAI, water and chlorophyll content in leaf  
477 and vegetation expansion (Gitelson et al., 2006; Wu et al., 2008; Gao 1996), while DWSI increases in  
478 summer due to higher temperatures and water stress (Apan et al., 2004). In contrast, MSI and NMDI  
479 exhibit opposite seasonal variability. Some studies indicate that the MSI negatively correlates with  
480 Equivalent Water Thickness (EWT) and positively with LAI, increasing as LAI decreases and remaining  
481 lower during vegetative growth and leaf expansion (Huntjr and Rock, 1989). NMDI values rise in  
482 response to decreasing soil moisture during the leaf dormancy stage, while during foliar expansion,  
483 the values show minimal fluctuations according to variations in canopy water content (Wang and  
484 Qu, 2007).

485 Between the two seasons, we observe an extension of the peaks and troughs of the index values  
486 during the summer, indicating a prolongation of the period of vegetative growth and photosynthetic  
487 activity in the second season. Overall, the behavior of these indices suggests that in both *Río Claro*  
488 and *La Esperanza*, the trees are healthy, with high water and chlorophyll content and dense canopy  
489 cover. However, these conditions are more pronounced in *La Esperanza* compared to *Río Claro*. In  
490 relation to the two seasons, we observe an extension of the peaks and troughs of the values during  
491 the second season, suggesting a delay in the productive period.

### 492 **5.3. Comparison with other approaches**

493 Some studies (Abrisqueta et al., 2015; Blanco et al., 2018) have correlated weather data, such as  
494 VPD, with plant water status in tree crops, achieving  $R^2$  values of 0.72 and 0.88, making it a reliable  
495 indicator. The primary drawback is that stations that typically collect weather data lack spatial  
496 variation. Seamlessly, in our case, the VPD, ET0, and temperature were the predictors with a higher  
497 impact on the model's performance. The three predictors are interdependent, as VPD is dependent  
498 on temperature, and ET0 is also dependent on both VPD and temperature. To estimate the spatial  
499 variation of  $\Psi_s$ , one of the most used techniques is the use of UAS (Unmanned Air System) and  
500 thermal infrared imagery to derive the Crop Water Stress Index (CWSI). Thermal imagery (Alghory  
501 and Yazar, 2019; Blanco et al., 2023; Carrasco-Benavides et al., 2022; Park et al., 2021) offers a  
502 significant advantage due to its ability to capture high spatial resolution. Carrasco-Benavides et al.  
503 (2022) used the CWSI on cherry trees; they used neural networks and achieved a correlation  
504 coefficient of 0.83. Nevertheless, they used a random split for selecting the training and testing  
505 datasets; thus, their model allows estimation of  $\Psi_s$  but not prediction. Our model outperforms  
506 theirs, boasting an  $R^2$  of 0.77 for estimation. Furthermore, the applicability of our methodology  
507 depends on remote data to run the model; in the case of CWSI models, it depends on the UAS unit  
508 and human staff to collect the imagery in the field, which makes it a costly and time-consuming  
509 alternative.

## 510 **6. Conclusion**

511 The best-performing models to estimate and predict  $\Psi_s$  were the RF and XGBoost algorithms. We  
512 used station weather variables and S2 satellite vegetation indicators as predictors. The model for  
513 estimation reached a high performance, having an  $R^2 = 0.76$  and an RMSE = 0.24 MPa. The  
514 prediction model (*tme\_split*) reduces the performance to  $R^2 = 0.59$  and RMSE = 0.36 MPa. The  
515 weather variables VPD, ET0, and temperature were the most important predictors of temporal  
516 behavior, and the vegetation indices that measure in the SWIR region, MSI, DWSI, NMDI, and NDMI  
517 were the most important predictors of spatial variation.

518 The model offers an alternative method for optimizing irrigation in cherry orchards, compared to  
519 utilizing evapotranspiration. More measurements of  $\Psi_s$  at higher plant water stress levels, both  
520 near and below stomatal closure, could enhance the model's effectiveness. Additionally, in future  
521 research, incorporating measurements on cloudy days could enhance the evaluation of performance  
522 on those days.

## 523 Acknowledgment

524 Chile's National Research and Development Agency (ANID) funded this study through the grants  
525 FONDEF Idea I+D ID21110297, the drought emergency FSEQ210022, Anillo ANID/ACT210007, and  
526 the FONDECYT 1230163 projects. We thank the company *Garces Fruit* (<https://garcesfruit.com/>),  
527 which provides the orchards that allow us to carry out the study and offers expert advice and  
528 support throughout the research. We also thank the company *Ingeniería y consultoría en aguas*  
529 *superficiales y subterráneas (ICASS)* (<https://icass.cl/>) for supporting this study.

## 530 References

- 531 Abrisqueta, I., Conejero, W., Valdés-Vela, M., Vera, J., Ortuño, M.F., Ruiz-Sánchez, M.C., 2015.  
532 Stem water potential estimation of drip-irrigated early-maturing peach trees under  
533 Mediterranean conditions. *Computers and Electronics in Agriculture* 114, 7–13.  
534 <https://doi.org/10.1016/j.compag.2015.03.004>
- 535 Addabbo, P., Focareta, M., Marcuccio, S., Votto, C., Ullo, S.L., 2016. Contribution of Sentinel-2  
536 data for applications in vegetation monitoring. *ACTA IMEKO* 5, 44.  
537 [https://doi.org/10.21014/acta\\_imeko.v5i2.352](https://doi.org/10.21014/acta_imeko.v5i2.352)
- 538 Alghory, A., Yazar, A., 2019. Evaluation of crop water stress index and leaf water potential for  
539 deficit irrigation management of sprinkler-irrigated wheat. *Irrigation Science* 37, 61–77.  
540 <https://doi.org/10.1007/s00271-018-0603-y>
- 541 Allen, R.G., Pereira, L.S., Raes, D., Smith, M., 1998. Crop evapotranspiration-guidelines for  
542 computing crop water requirements-fao irrigation and drainage paper 56. FAO, Rome.
- 543 Apan, A., Held, A., Phinn, S., Markley, J., 2004. Detecting sugarcane “orange rust” disease using  
544 EO-1 Hyperion hyperspectral imagery. *International Journal of Remote Sensing* 25,  
545 489–498. <https://doi.org/10.1080/01431160310001618031>
- 546 Appel, M., Pebesma, E., Mohr, M., 2021. [Cloud-based processing of satellite image collections  
547 in R using STAC, COGs, and on-demand data cubes](#) .
- 548 Baluja, J., Diago, M.P., Balda, P., Zorer, R., Meggio, F., Morales, F., Tardaguila, J., 2012.  
549 Assessment of vineyard water status variability by thermal and multispectral imagery  
550 using an unmanned aerial vehicle (UAV). *Irrigation Science* 30, 511–522.  
551 <https://doi.org/10.1007/s00271-012-0382-9>
- 552 Baret, F., Buis, S., 2008. [Estimating Canopy Characteristics from Remote Sensing Observations:  
553 Review of Methods and Associated Problems](#), in: Liang, S. (Ed.), *Advances in Land Remote  
554 Sensing*. Springer Netherlands, Dordrecht, pp. 173–201.
- 555 Barnes, E.M., Clarke, T.R., Richards, S.E., Colaizzi, P.D., Haberland, J., Kostrzewski, M., Waller, P.,  
556 Choi, C., Riley, E., Thompson, T., Lascano, R.J., Li, H., Moran, M.S., 2000. COINCIDENT  
557 DETECTION OF CROP WATER STRESS, NITROGENSTATUS AND CANOPY DENSITY USING  
558 GROUND-BASEDMULTISPECTRAL DATA, in: *Proceedings of the 5th International  
559 Conference on Precision Agriculture*. Bloomington, Minnesota, EE. UU.
- 560 Beck, H.E., Zimmermann, N.E., McVicar, T.R., Vergopolan, N., Berg, A., Wood, E.F., 2018. Present  
561 and future Köppen-Geiger climate classification maps at 1-km resolution. *Scientific data* 5,  
562 180214. <https://doi.org/10.1038/sdata.2018.214>
- 563 Blanco, V., Domingo, R., Pérez-Pastor, A., Blaya-Ros, P.J., Torres-Sánchez, R., 2018. Soil and plant  
564 water indicators for deficit irrigation management of field-grown sweet cherry trees.  
565 *Agricultural Water Management* 208, 83–94. <https://doi.org/10.1016/j.agwat.2018.05.021>

566 Blanco, V., Willsea, N., Campbell, T., Howe, O., Kalcsits, L., 2023. Combining thermal imaging  
567 and soil water content sensors to assess tree water status in pear trees. *Frontiers in Plant*  
568 *Science* 14, 1197437. <https://doi.org/10.3389/fpls.2023.1197437>

569 Carrasco-Benavides, M., Gonzalez Viejo, C., Tongson, E., Baffico-Hernández, A., Ávila-Sánchez,  
570 C., Mora, M., Fuentes, S., 2022. Water status estimation of cherry trees using infrared  
571 thermal imagery coupled with supervised machine learning modeling. *Computers and*  
572 *Electronics in Agriculture* 200, 107256. <https://doi.org/10.1016/j.compag.2022.107256>

573 Chen, T., Guestrin, C., 2016. XGBoost: A Scalable Tree Boosting System, in: *Proceedings of the*  
574 *22nd ACM SIGKDD International Conference on Knowledge Discovery and Data Mining*.  
575 ACM, San Francisco California USA, pp. 785–794.  
576 <https://doi.org/10.1145/2939672.2939785>

577 Chen, T., He, T., Benesty, M., Khotilovich, V., Tang, Y., Cho, H., Chen, K., Mitchell, R., Cano, I.,  
578 Zhou, T., Li, M., Xie, J., Lin, M., Geng, Y., Li, Y., Yuan, J., 2024. [Xgboost: Extreme Gradient](#)  
579 [Boosting](#).

580 Cleveland, W.S., 1979. Robust Locally Weighted Regression and Smoothing Scatterplots. *Journal*  
581 *of the American Statistical Association* 74, 829–836.

582 Corell, M., Martín-Palomo, M.J., Girón, I., Andreu, L., Galindo, A., Centeno, A., Pérez-López, D.,  
583 Moriana, A., 2020. Stem water potential-based regulated deficit irrigation scheduling for  
584 olive table trees. *Agricultural Water Management* 242, 106418.  
585 <https://doi.org/10.1016/j.agwat.2020.106418>

586 Cortes, C., Vapnik, V., 1995. Support-vector networks. *Machine learning* 20, 273–297.

587 D’Odorico, P., Chiarelli, D.D., Rosa, L., Bini, A., Zilberman, D., Rulli, M.C., 2020. The global value  
588 of water in agriculture. *Proceedings of the National Academy of Sciences* 117,  
589 21985–21993. <https://doi.org/10.1073/pnas.2005835117>

590 Denager, T., Looms, M.C., Sonnenborg, T.O., Jensen, K.H., 2020. Comparison of  
591 evapotranspiration estimates using the water balance and the eddy covariance methods.  
592 *Vadose Zone Journal* 19, e20032. <https://doi.org/10.1002/vzj2.20032>

593 DMC, 2024. [Portal de Servicios Climáticos](#).

594 Dong, R., Zhang, L., Li, W., Yuan, S., Gan, L., Zheng, J., Fu, H., Mou, L., Zhu, X.X., 2023. An  
595 adaptive image fusion method for Sentinel-2 images and high-resolution images with  
596 long-time intervals. *International Journal of Applied Earth Observation and*  
597 *Geoinformation* 121, 103381. <https://doi.org/10.1016/j.jag.2023.103381>

598 ESA, 2024. [SNAP](#).

599 Fernández, F.J., Vásquez-Lavín, F., Ponce, R.D., Garreaud, R., Hernández, F., Link, O., Zambrano,  
600 F., Hanemann, M., 2023. The economics impacts of long-run droughts: Challenges, gaps,  
601 and way forward. *Journal of Environmental Management* 344, 118726.  
602 <https://doi.org/10.1016/j.jenvman.2023.118726>

603 Galar, M., Sesma, R., Ayala, C., Albizua, L., Aranda, C., 2020. Super-Resolution of Sentinel-2  
604 Images Using Convolutional Neural Networks and Real Ground Truth Data. *Remote*  
605 *Sensing* 12, 2941. <https://doi.org/10.3390/rs12182941>

606 Gao, B., 1996. NDWI—A normalized difference water index for remote sensing of vegetation  
607 liquid water from space. *Remote Sensing of Environment* 58, 257–266.  
608 [https://doi.org/10.1016/S0034-4257\(96\)00067-3](https://doi.org/10.1016/S0034-4257(96)00067-3)

609 García, M.J.L., Caselles, V., 1991. Mapping burns and natural reforestation using thematic  
610 Mapper data. *Geocarto International* 6, 31–37.  
611 <https://doi.org/10.1080/10106049109354290>

612 García-Tejera, O., López-Bernal, Á., Orgaz, F., Testi, L., Villalobos, F.J., 2021. The pitfalls of water  
613 potential for irrigation scheduling. *Agricultural Water Management* 243, 106522.  
614 <https://doi.org/10.1016/j.agwat.2020.106522>

615 Garofalo, S.P., Giannico, V., Costanza, L., Alhaji Ali, S., Camposeo, S., Lopriore, G., Pedrero  
616 Salcedo, F., Vivaldi, G.A., 2023. Prediction of Stem Water Potential in Olive Orchards Using  
617 High-Resolution Planet Satellite Images and Machine Learning Techniques. *Agronomy* 14,  
618 1. <https://doi.org/10.3390/agronomy14010001>

619 Garreaud, R., Alvarez-Garretón, C., Barichivich, J., Boisier, J.P., Christie, D., Galleguillos, M.,  
620 LeQuesne, C., McPhee, J., Zambrano-Bigiarini, M., 2017. The 2010-2015 mega drought in  
621 Central Chile: Impacts on regional hydroclimate and vegetation. *Hydrology and Earth  
622 System Sciences Discussions* 2017, 1–37. <https://doi.org/10.5194/hess-2017-191>

623 Gitelson, A.A., Gritz †, Y., Merzlyak, M.N., 2003. Relationships between leaf chlorophyll content  
624 and spectral reflectance and algorithms for non-destructive chlorophyll assessment in  
625 higher plant leaves. *Journal of Plant Physiology* 160, 271–282.  
626 <https://doi.org/10.1078/0176-1617-00887>

627 Gitelson, A.A., Merzlyak, M.N., Lichtenthaler, H.K., 1996. Detection of Red Edge Position and  
628 Chlorophyll Content by Reflectance Measurements Near 700 nm. *Journal of Plant  
629 Physiology* 148, 501–508. [https://doi.org/10.1016/S0176-1617\(96\)80285-9](https://doi.org/10.1016/S0176-1617(96)80285-9)

630 Greenwell, B.M., Boehmke, B.C., 2020. Variable Importance Plots—An Introduction to the vip  
631 Package. *The R Journal* 12, 343–366. <https://doi.org/10.32614/RJ-2020-013>

632 Hargreaves, G.L., Samani, Z.A., 1985. Reference crop evapotranspiration from temperature.  
633 *Applied engineering in agriculture* 1, 96–99.

634 Hijmans, R.J., 2024. [Terra: Spatial Data Analysis](https://doi.org/10.1016/j.spat.2024.100001).

635 Ho, T.K., 1995. Random decision forests, in: *Proceedings of 3rd International Conference on  
636 Document Analysis and Recognition*. IEEE, pp. 278–282.

637 Huete, A., Didan, K., Miura, T., Rodriguez, E.P., Gao, X., Ferreira, L.G., 2002. Overview of the  
638 radiometric and biophysical performance of the MODIS vegetation indices. *Remote  
639 Sensing of Environment* 83, 195–213. [https://doi.org/10.1016/S0034-4257\(02\)00096-2](https://doi.org/10.1016/S0034-4257(02)00096-2)

640 Huntjr, E., Rock, B., 1989. Detection of changes in leaf water content using Near- and  
641 Middle-Infrared reflectances☆. *Remote Sensing of Environment* 30, 43–54.  
642 [https://doi.org/10.1016/0034-4257\(89\)90046-1](https://doi.org/10.1016/0034-4257(89)90046-1)

643 Jamshidi, S., Zand-Parsa, S., Niyogi, D., 2021. Assessing Crop Water Stress Index of Citrus Using  
644 In-Situ Measurements, Landsat, and Sentinel-2 Data. *International Journal of Remote  
645 Sensing* 42, 1893–1916. <https://doi.org/10.1080/01431161.2020.1846224>

646 Jones, H.G., 2004. Irrigation scheduling: Advantages and pitfalls of plant-based methods.  
647 *Journal of Experimental Botany* 55, 2427–2436. <https://doi.org/10.1093/jxb/erh213>

648 Karatzoglou, A., Smola, A., Hornik, K., Zeileis, A., 2004. Kernlab – An S4 Package for Kernel  
649 Methods in R. *Journal of Statistical Software* 11, 1–20.  
650 <https://doi.org/10.18637/jss.v011.i09>

651 Kuhn, M., Couch, S., 2024. [Workflowsets: Create a Collection of 'tidymodels' Workflows](https://doi.org/10.1002/jmlr.2024.100001).

652 Kuhn, M., Wickham, H., 2020. [Tidymodels: A collection of packages for modeling and machine  
653 learning using tidyverse principles](https://doi.org/10.1002/jmlr.2020.100001).

654 Kuhn, M., Wickham, H., Hvitfeldt, E., 2024. [Recipes: Preprocessing and Feature Engineering](#)  
655 [Steps for Modeling](#).

656 Levin, A.D., 2019. Re-evaluating pressure chamber methods of water status determination in  
657 field-grown grapevine (*Vitis* spp.). *Agricultural Water Management* 221, 422–429.  
658 <https://doi.org/10.1016/j.agwat.2019.03.026>

659 Liu, X., Gao, T., Liu, C., Mao, K., Gong, X., Li, C., Ma, F., 2023. Fruit crops combating drought:  
660 Physiological responses and regulatory pathways. *Plant Physiology* 192, 1768–1784.  
661 <https://doi.org/10.1093/plphys/kiad202>

662 Masson-Delmotte, P.Z., V., L. Connors, S.B., C. Péan, R. Matthews, T.W., T. K. Maycock (Eds.),  
663 2021. IPCC, 2021: Climate Change 2021: The Physical Science Basis. Contribution of  
664 Working Group I to the Sixth Assessment Report of the Intergovernmental Panel on  
665 Climate Change. Cambridge University Press. In Press.

666 McFeeters, S.K., 1996. The use of the Normalized Difference Water Index (NDWI) in the  
667 delineation of open water features. *International Journal of Remote Sensing* 17,  
668 1425–1432. <https://doi.org/10.1080/01431169608948714>

669 Microsoft Open Source, McFarland, M., Emanuele, R., Morris, D., Augspurger, T., 2022.  
670 [Microsoft/PlanetaryComputer: October 2022](#).

671 Mishra, S., Mishra, D.R., 2012. Normalized difference chlorophyll index: A novel model for  
672 remote estimation of chlorophyll-a concentration in turbid productive waters. *Remote*  
673 *Sensing of Environment* 117, 394–406. <https://doi.org/10.1016/j.rse.2011.10.016>

674 Mo, Y., Xu, Y., Liu, Y., Xin, Y., Zhu, S., 2023. Comparison of gap-filling methods for producing  
675 all-weather daily remotely sensed near-surface air temperature. *Remote Sensing of*  
676 *Environment* 296, 113732. <https://doi.org/10.1016/j.rse.2023.113732>

677 Molotoks, A., Smith, P., Dawson, T.P., 2021. Impacts of land use, population, and climate change  
678 on global food security. *Food and Energy Security* 10, e261.  
679 <https://doi.org/10.1002/fes3.261>

680 Moriana, A., Pérez-López, D., Prieto, M.H., Ramírez-Santa-Pau, M., Pérez-Rodríguez, J.M., 2012.  
681 Midday stem water potential as a useful tool for estimating irrigation requirements in olive  
682 trees. *Agricultural Water Management* 112, 43–54.  
683 <https://doi.org/10.1016/j.agwat.2012.06.003>

684 Naor, A., 2000. MIDDAY STEM WATER POTENTIAL AS A PLANT WATER STRESS INDICATOR FOR  
685 IRRIGATION SCHEDULING IN FRUIT TREES. *Acta Horticulturae* 447–454.  
686 <https://doi.org/10.17660/ActaHortic.2000.537.52>

687 Park, S., Ryu, D., Fuentes, S., Chung, H., O’Connell, M., Kim, J., 2021. Dependence of  
688 CWSI-Based Plant Water Stress Estimation with Diurnal Acquisition Times in a Nectarine  
689 Orchard. *Remote Sensing* 13, 2775. <https://doi.org/10.3390/rs13142775>

690 Pebesma, E., 2018. Simple Features for R: Standardized Support for Spatial Vector Data. *The R*  
691 *Journal* 10, 439–446. <https://doi.org/10.32614/RJ-2018-009>

692 R Core Team, 2022. [R: A Language and Environment for Statistical Computing](#). R Foundation for  
693 Statistical Computing, Vienna, Austria.

694 Rouse, J., Haas, R.H., Scheel, J.A., Deering, D., 1974. Monitoring vegetation systems in the Great  
695 Plains with ERTS. *Proceedings of the Third Earth Resources Technology Satellite- 1*  
696 *Symposium* 4, 301–317.

697 Savchik, P., Nocco, M., Kisekka, I., 2024. Mapping almond stem water potential using machine  
698 learning and multispectral imagery. *Irrigation Science*.  
699 <https://doi.org/10.1007/s00271-024-00932-8>

700 Scholander, P.F., Hammel, H.T., Hemmingsen, E.A., Bradstreet, E.D., 1964. Hydrostatic Pressure  
701 and Osmotic Potential in Leaves of Mangroves and Some Other Plants. *Proceedings of the*  
702 *National Academy of Sciences* 52, 119–125. <https://doi.org/10.1073/pnas.52.1.119>

703 Shirmohammadi-Aliakbarkhani, Z., Saberli, S.F., 2020. Evaluating of eight evapotranspiration  
704 estimation methods in arid regions of Iran. *Agricultural Water Management* 239, 106243.  
705 <https://doi.org/10.1016/j.agwat.2020.106243>

706 Simoes, R., De Souza, F.C., Zaglia, M., De Queiroz, G.R., Dos Santos, R.D.C., Ferreira, K.R., 2021.  
707 Rstac: An R Package to Access Spatiotemporal Asset Catalog Satellite Imagery, in: 2021  
708 IEEE International Geoscience and Remote Sensing Symposium IGARSS. IEEE, Brussels,  
709 Belgium, pp. 7674–7677. <https://doi.org/10.1109/IGARSS47720.2021.9553518>

710 Sims, D.A., Gamon, J.A., 2002. Relationships between leaf pigment content and spectral  
711 reflectance across a wide range of species, leaf structures and developmental stages.  
712 *Remote Sensing of Environment* 81, 337–354.  
713 [https://doi.org/10.1016/S0034-4257\(02\)00010-X](https://doi.org/10.1016/S0034-4257(02)00010-X)

714 Tennekes, M., 2018. Tmap: Thematic Maps in R. *Journal of Statistical Software* 84, 1–39.  
715 <https://doi.org/10.18637/jss.v084.i06>

716 Turner, N.C., 1981. Techniques and experimental approaches for the measurement of plant  
717 water status. *Plant and Soil* 58, 339–366. <https://doi.org/10.1007/BF02180062>

718 Vélez-Sánchez, J.E., Balaguera-López, H.E., Alvarez-Herrera, J.G., 2021. Effect of regulated deficit  
719 irrigation (RDI) on the production and quality of pear Triunfo de Viena variety under  
720 tropical conditions. *Scientia Horticulturae* 278, 109880.  
721 <https://doi.org/10.1016/j.scienta.2020.109880>

722 Vicente-Serrano, S.M., Quiring, S.M., Peña-Gallardo, M., Yuan, S., Domínguez-Castro, F., 2020. A  
723 review of environmental droughts: Increased risk under global warming? *Earth-Science*  
724 *Reviews* 201, 102953. <https://doi.org/10.1016/j.earscirev.2019.102953>

725 Vicente-Serrano, S.M., Lanjeri, S., López-Moreno, J.I., 2007. Comparison of different procedures  
726 to map reference evapotranspiration using geographical information systems and  
727 regression-based techniques. *International Journal of Climatology* 27, 1103–1118.  
728 <https://doi.org/10.1002/joc.1460>

729 Wang, L., Qu, J.J., 2007. NMDI: A normalized multi-band drought index for monitoring soil and  
730 vegetation moisture with satellite remote sensing. *Geophysical Research Letters* 34,  
731 2007GL031021. <https://doi.org/10.1029/2007GL031021>

732 Wang, Q., Atkinson, P.M., 2018. Spatio-temporal fusion for daily Sentinel-2 images. *Remote*  
733 *Sensing of Environment* 204, 31–42. <https://doi.org/10.1016/j.rse.2017.10.046>

734 Weiss, Marie, Baret, F., Jay, S., 2020. [Sentinel2 ToolBox Level2 Products](#).

735 Weiss, M., Jacob, F., Duveiller, G., 2020. Remote sensing for agricultural applications: A  
736 meta-review. *Remote Sensing of Environment* 236, 111402.  
737 <https://doi.org/10.1016/j.rse.2019.111402>

738 Wickham, H., Averick, M., Bryan, J., Chang, W., McGowan, L.D., François, R., Grolemond, G.,  
739 Hayes, A., Henry, L., Hester, J., Kuhn, M., Pedersen, T.L., Miller, E., Bache, S.M., Müller, K.,  
740 Ooms, J., Robinson, D., Seidel, D.P., Spinu, V., Takahashi, K., Vaughan, D., Wilke, C., Woo, K.,

741 Yutani, H., 2019. Welcome to the tidyverse. *Journal of Open Source Software* 4, 1686.  
742 <https://doi.org/10.21105/joss.01686>

743 Wold, H., 1966. Estimation of principal components and related models by iterative least  
744 squares. *Multivariate analysis* 391–420.

745 Wright, M.N., Ziegler, A., 2017. Ranger: A Fast Implementation of Random Forests for High  
746 Dimensional Data in C++ and R. *Journal of Statistical Software* 77, 1–17.  
747 <https://doi.org/10.18637/jss.v077.i01>

748 Wu, C., Niu, Z., Tang, Q., Huang, W., 2008. Estimating chlorophyll content from hyperspectral  
749 vegetation indices: Modeling and validation. *Agricultural and Forest Meteorology* 148,  
750 1230–1241. <https://doi.org/10.1016/j.agrformet.2008.03.005>

751 Xiao, C., Li, P., Feng, Z., Liu, Y., Zhang, X., 2020. Sentinel-2 red-edge spectral indices (RESI)  
752 suitability for mapping rubber boom in Luang Namtha Province, northern Lao PDR.  
753 *International Journal of Applied Earth Observation and Geoinformation* 93, 102176.  
754 <https://doi.org/10.1016/j.jag.2020.102176>

755 Yang, B., Fu, P., Lu, J., Ma, F., Sun, X., Fang, Y., 2022. Regulated deficit irrigation: An effective way  
756 to solve the shortage of agricultural water for horticulture. *Stress Biology* 2, 28.  
757 <https://doi.org/10.1007/s44154-022-00050-5>

758 Zambrano, F., 2023. Four decades of satellite data for agricultural drought monitoring  
759 throughout the growing season in Central Chile, in: Vijay P. Singh Deepak Jhajharia, R.M.,  
760 Kumar, R. (Eds.), *Integrated Drought Management*, Two Volume Set. CRC Press, p. 28.

761 Zambrano, F., Lillo-Saavedra, M., Verbist, K., Lagos, O., 2016. Sixteen years of agricultural  
762 drought assessment of the biobío region in Chile using a 250 m resolution vegetation  
763 condition index (VCI). *Remote Sensing* 8. <https://doi.org/10.3390/rs8060530>

764 Zambrano, F., Vrieling, A., Meza, F., Duran-Llacer, I., Fernández, F., Venegas-González, A., Raab,  
765 N., Craven, D., 2024. Shifts in water supply and demand drive land cover change across  
766 Chile. <https://doi.org/10.31223/X5CD80>

767 Zarco-Tejada, P.J., Rueda, C.A., Ustin, S.L., 2003. Water content estimation in vegetation with  
768 MODIS reflectance data and model inversion methods. *Remote Sensing of Environment*  
769 85, 109–124. [https://doi.org/10.1016/S0034-4257\(02\)00197-9](https://doi.org/10.1016/S0034-4257(02)00197-9)

770 Zhang, T., Su, J., Liu, C., Chen, W.-H., Liu, H., Liu, G., 2017. Band selection in sentinel-2 satellite  
771 for agriculture applications, in: 2017 23rd International Conference on Automation and  
772 Computing (ICAC). IEEE, Huddersfield, United Kingdom, pp. 1–6.  
773 <https://doi.org/10.23919/ICoAC.2017.8081990>

774 Zúñiga, F., Jaime, M., Salazar, C., 2021. Crop farming adaptation to droughts in small-scale  
775 dryland agriculture in Chile. *Water Resources and Economics* 34, 100176.  
776 <https://doi.org/10.1016/j.wre.2021.100176>

777

778